Strain evolution during hydride precipitation in Zircaloy-4 observed with synchrotron X-ray diffraction

M.S. Blackmur [a, *], M. Preuss [a], J.D. Robson [a], O. Zanellato [b], R.J. Cernik [a], F. Ribeiro [c], J. Andrieux [d, e]

[a] Materials Performance Centre, School of Materials, The University of Manchester, Manchester, M1 7HS, United Kingdom
[b] PIMM, Ensam – Cnam – CNRS, 151 Boulevard de l'Hôpital, 75013, Paris, France
[c] Institut de Radioprotection et de Sûreté Nucléaire, CEN Cadarache, 13115, St. Paul Les Durance, France
[d] Beamline ID15, European Synchrotron Radiation Facility, 6 rue J Horowitz, 38043, Grenoble, France
[e] Laboratoire des Multimatériaux et Interfaces, Université de Lyon, 43 Bd du 11 novembre 1918, Villeurbanne, 69100, France

HIGHLIGHTS

- Strain evolution was studied in matrix and δ-hydride using synchrotron X-ray diffraction during isothermal precipitation and thermal ramps at reactor-relevant temperatures.
- Thermally, chemically and mechanically induced strains were deconvoluted in the matrix, indicating the effect of hydrides on matrix strain evolution.
- A slow strain rate relaxation of elastic strains was observed, suggesting a time-dependent stress relaxation mechanism at reactor relevant temperatures.
- Anisotropy in matrix strain evolution between the $<1120>_\alpha$ and $<1100>_\alpha$ directions supports observations by others of anisotropic misfit from hydride precipitation in these directions.
- A thermal effect on hydride constraint was also observed, possibly indicating that lattice dilatation from interstitial hydrogen may reduce misfit stresses experienced by hydride precipitates.

ARTICLE INFO

Article history:
Received 18 May 2015
Received in revised form
28 January 2016
Accepted 30 January 2016
Available online 26 February 2016

Keywords:
Synchrotron X-ray diffraction
Hydride precipitation
Zirconium alloys
Strain evolution

ABSTRACT

Synchrotron X-ray diffraction was used to evaluate strain evolution observed in Zircaloy-4 undergoing hydride precipitation during a range of thermal operations. During continuous heating, a change in the constraining effect of the matrix was observed at a temperature of 280 °C, thought to be the result of matrix dilatation from interstitial hydrogen. A deconvolution of the thermal, chemical and mechanical sources of strain during quench and dwell operations identified a non-negligible mechanical effect in the matrix. During these dwells, slow strain rate relaxation of elastic strains was seen in the matrix and hydride, suggesting that time dependent relaxation of misfit stresses may be possible at reactor relevant temperatures. Notable anisotropy was observed between the rolling and transverse directions, identified as being the likely product of a similar anisotropy in the relaxation of the hydride misfit between the $<11\bar{2}0>_\alpha$ and $<1\bar{1}00>_\alpha$ matrix directions, owing to the differing coherency of these two interfaces.

1. Introduction

Since the early days of defence and civil nuclear energy, zirconium alloys have been ubiquitous as a structural material in water-cooled reactor cores owing to their low cross section for neutron absorption, aqueous corrosion resistance and mechanical properties at elevated temperatures [1,2]. The corrosion that does take place, however, generates hydrogen as a product of the oxidation reaction, and zirconium has a strong propensity to absorb a fraction of this [3,4]. Once within the material, the precipitation of hydrogen into hydrides is governed by the local solubility, where thermal gradients across components can lead to solubility gradients, and thus non-uniform hydride distributions [5].

Taking coolant temperature to be representative of that of zirconium cladding (at the outer surface, at least), a representative Pressurised Water Reactor (PWR) might see inlet and outlet

* Corresponding author. Materials Performance Centre, School of Materials, The University of Manchester, Manchester, M13 9PL, United Kingdom.
E-mail address: matthew.blackmur@alumni.manchester.ac.uk (M.S. Blackmur).

http://dx.doi.org/10.1016/j.jnucmat.2016.01.039

temperatures of approximately 290 °C and 323 °C, respectively [6]. Given this operating range, the maximum solubility for hydrogen would be around 143 $ppm_{wt.}$ [7], compared to a bulk hydrogen content of approximately 290 $ppm_{wt.}$ after a common service life burn up of 44 GWd/t_U for Zircaloy-4 [8]. In fact, hydrogen pick-up curves for this alloy suggest that the hydrogen content of fuel cladding exposed to coolant at 323 °C could potentially reach the precipitation solubility limit after just 23.3 GWd/t_U, assuming a simplistic uniform hydrogen distribution [6–8]. Where temperature decreases occur, during thermal transients or refuelling shutdowns for example, the solubility falls rapidly. At ambient temperatures the solubility of hydrogen in zirconium is less than 1 $ppm_{wt.}$ [7], and almost all hydrogen will rapidly precipitate into hydrides.

Once formed, this brittle phase has been shown to degrade the bulk mechanical properties of zirconium cladding [9–16] and introduce mechanisms for failure through Delayed Hydride Cracking (DHC), secondary hydriding and hydride blistering [17–23]. As such, a strong understanding of the impact of hydrides on zirconium alloys is critical to ensure the integrity of nuclear fuel assemblies is maintained during service life and storage. This will become even more critical in the future, where any extension of fuel assemblage burn-up may lead to a notable hydrogen content increase in end of life components [8].

Numerous studies have sought to quantify the zirconium–hydrogen system, although the complex nature of the processes involved means many areas are still unclear [24–26]. The most widely observed and discussed phase is the non-stoichiometric face-centered cubic δ-$ZrH_{\approx 1.66}$ hydride, considered the stable phase at room temperature by most researchers [27,28]. However, additional complexity arises since the face-centered tetragonal γ-phase is thought to be metastable alongside stable δ-hydride or even entirely stable itself, as a function of cooling rate, hydrogen concentration and alloy composition [29–33]. Given the metastable nature of γ, the balance between the two phases can be influenced by external factors and both phases can also coexist. For example, stress stabilisation of γ has been recorded [27] and γ-tipped, δ-cored precipitates have been observed [34]. Examples of ε- and ζ-hydride phases have also been reported in the literature, however, the precise conditions of their formation are still somewhat unclear, aside from high concentrations of hydrogen [35–39].

Irrespective of which hydride phase forms, the zirconium–zirconium hydride transformation is associated with a volume expansion, owing to the lower physical density of hydrides, and so newly formed precipitates have an associated misfit with their parent lattice [34,40,41]. Discrepancies exist in the literature between theoretically predicted transformation strains [41] and experimentally measured (post-plastic relaxation) [34] interfacial strains for δ, and so its morphology is generally reported to be either needle-like or that of a platelet, based on the anisotropic misfit with the parent matrix. The needle morphology may develop as a function of the anisotropic relaxation of the misfit strains during the growth phase of precipitation [34]. This would then have the potential to cause hydrogen to be preferentially drawn up the stress gradient [42] towards the edges in the $<11\bar{2}0>_\alpha$ directions, where stresses would be higher than those in $<1\bar{1}00>_\alpha$, encouraging the formation of needles. When precipitating, the strain field and dislocation structures surrounding hydrides, generated by the particle-matrix misfit, are thought to encourage the sympathetic nucleation of 'daughter' hydrides [33,43–46]. This is owing to the trapping of hydrogen within lattice defects [44] or a lowering of the elastic accommodation energy by the tensile stresses that a misfitting hydride will generate in the surrounding matrix [43,46]. These daughter hydrides often stack or chain to form the comparatively large hydride regions observed through optical microscopy, which can appear to be a single very large hydride [47–51]. The orientation, distribution and morphology of these larger hydride regions is the product of numerous factors, including thermal history, component stress state, microstructure and texture [40]. That said, the micro-hydrides, which constitute them, predominantly display an orientation relationship of $(0001)_\alpha \parallel (111)_\delta$ with the parent lattice [40,48,52] and will always precipitate with the platelet normal parallel to the matrix basal normal.

The generated misfit is also thought to impact on the terminal solid solubility of hydrogen in zirconium, where the additional undercooling required to precipitate the phase is reflective of the energy required to produce first elastic and then plastic deformation in the matrix and hydride [53–55]. Other work postulates that the hysteresis may even be an artefact seen where the concentration of hydrogen in solution has not reached equilibrium, owing to rate limited kinetics [51,56]. Given that the strain contribution to the energy barrier is thought to be second order to interfacial energy by some [57], the solubility curves recorded experimentally will also be heavily influenced by the energy associated with a change in interfaces.

Synchrotron X-ray Diffraction (SXRD) has grown as a major technique employed for investigating hydrides, owing to the large spatial, small temporal and sharp achievable angular resolutions. These studies cover a wide range of aspects and topics of the zirconium–hydrogen system, showcasing the diverse capabilities of modern synchrotron facilities. Some works have investigated thermal cycles and their effect on stresses and strains within the matrix and hydride, as well as hydrogen solubility and hydride nucleation [51,57,58]. Others have looked at hydride reorientation [40,59,60] or the impact of a notch and resulting stress-field on hydride precipitation and fracture [61,62]. Phase identification and quantification has been performed [35], phase diagrams have been constructed [33] and phase transformations have been observed [27]. The impact of the matrix on hydride formation has also been studied, where texture [55], mechanical properties and microstructure [63] have been shown as significant to the process.

The present work uses high-energy synchrotron X-ray diffraction to investigate the evolution of strain in both the matrix and hydride precipitates during a series of isothermal holds over a range of reactor-relevant temperatures. A model for matrix lattice distortion from dissolved hydrogen [51] is employed to deconvolute the components to strain evolution.

2. Experimental

2.1. Sample specification

The Zircaloy-4 sample utilised here was supplied by the Institut de Radioprotection et de Sûreté Nucléaire, France, and possessed the same processing history as the sheet material used in Ref. [51]. After rolling to 400 μm, the sample was cut to 50 mm × 5 mm in the rolling and transverse directions, respectively, and recrystallised [51]. EBSD analysis showed the material to possess an average grain size of 8–10 μm, with the expected split basal texture of rolled and recrystallised zirconium sheet material. In this, basal poles are normally tilted by ±20–40° from normal, where the secondary direction is determined by the c/a ratio [64]. The texture of this material is shown in Fig. 1(a), and the corresponding Kearns factors (details in Ref. [65]) are $f_{RD} = 0.120$, $f_{TD} = 0.248$ and $f_{ND} = 0.631$. The sample geometry and the relationship between the beam, detector and Rolling/Transverse/Normal Directions (RD/TD/ND, respectively) are presented schematically in Fig. 1(b).

After thermomechanical processing, hydrogen was charged into the sample using the methodology described by Zanellato et al.

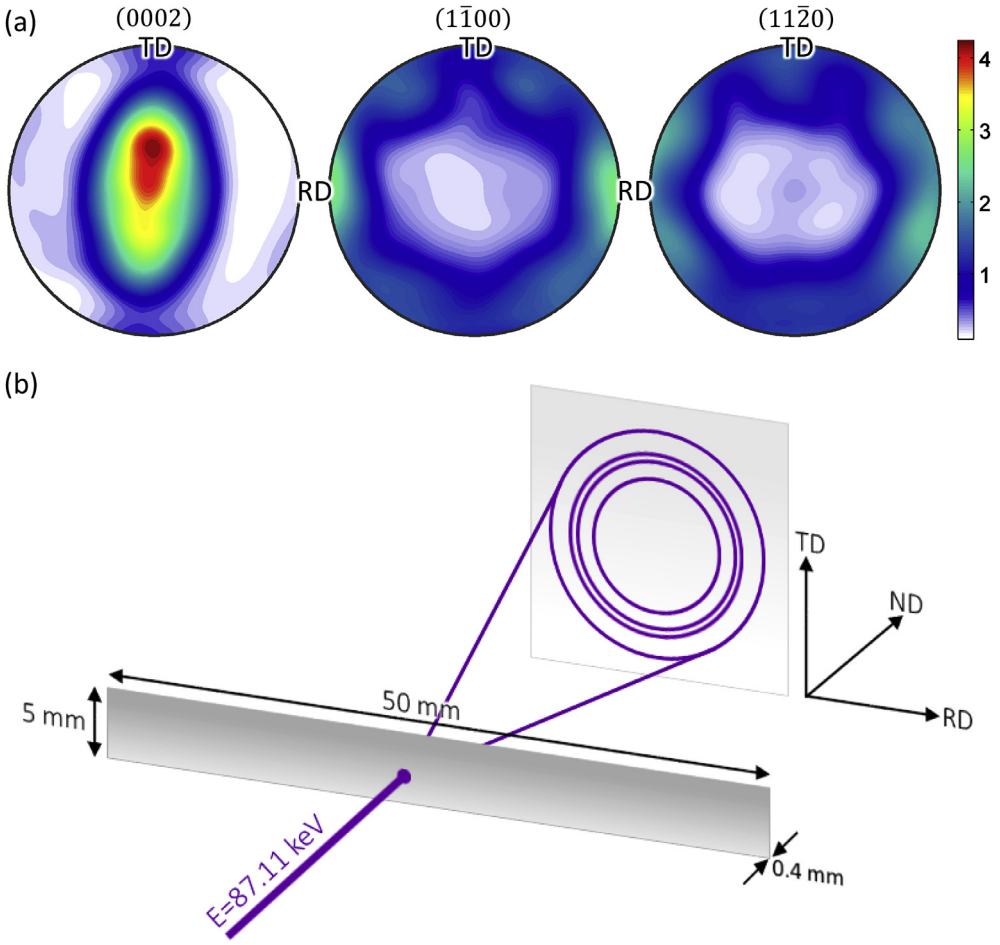

Fig. 1. (a) Recorded texture of rolled and recrystallised Zircaloy-4 sample, measured through EBSD orientation mapping, and (b) the sample geometry and RD/TD/ND relationship.

[51], and the concentration at the time of experimentation was 430 $ppm_{wt.}$, with a gradient of no more than 3 $ppm_{wt.}$ mm^{-1}. This was selected as the relatively high content of hydrogen produces a sufficiently large diffracting volume of hydrides within the sample, yielding more detectable diffraction signals. When compared with expected hydrogen contents in Zircaloy-4 cladding at the end of fuel assembly life, this value is similar to that found in components with 49 GWd/t_U burn-up; close to the end of life hydrogen content for some operators [8]. The size and quality of hydride reflections becomes important in the zirconium–hydride system; as while the angular resolution of synchrotron diffraction is good, there is still some overlap with the dominant matrix reflections or their tails.

2.2. Synchrotron X-ray diffraction parameters

The present experiment was undertaken at the European Synchrotron Radiation Facility (France), on beamline ID15B. This instrument is a high-energy diffraction beamline for which the full technical details are available in Refs. [66,67]. X-ray diffraction was performed under transmission (Debye–Scherrer) geometry, where the beam was incident orthogonally to the surface of the specimen. This allowed for the sampling of a large material volume, through the sheet thickness, yielding bulk measurements of hydrides within the sample. Diffraction patterns were imaged with a Trixell Pixium 4700 detector; where acquisitions were made over 5 s, followed by 4–5 s of disk write time. This resulted in a temporal resolution of 9–10 s per imaged Debye–Scherrer ring pattern. A monochromatic beam with a constant energy of $E = 87.17 \pm 0.01$ keV was used to illuminate the sample during this work, with a wavelength of $\lambda = 0.14223$ Å and beam size of 300 μm × 300 μm.

2.3. Thermal transients

Thermal operations were performed using resistive (Joule) heating, driven by an Electrothermal Mechanical Tester (ETMT8800), manufactured by Instron, in which the specimen was mounted. Sample temperature was monitored close to the beam (at the axial centre of the sample) using an S-Type thermocouple and the heating current was adjusted dynamically by the software to maintain desired temperatures. This was necessary to mitigate against heat loss to the water-cooled grips and chamber atmosphere. In addition, the ETMT control software was set to adjust the position of the mobile armature to maintain zero load on the sample, compensating for thermal expansion. Due to the high affinity of zirconium for oxygen at elevated temperatures, the chamber of the ETMT was purged with inert argon gas, which continued to flow through the chamber throughout the experiment.

The experimental programme involved a single ramped thermal operation, followed by seven quench and hold operations. Cycle 1 (C1) allowed for the measurement of solubility curves during heating and cooling at a continuous 1 °C s^{-1}, from a minimum temperature of 40 °C (T_{floor}) to a maximum of 570 °C (T_{max}), above the expected eutectoid temperature [68]. Given the hydrogen

content of the sample, the dissolution solubility was found to be 429 °C, and for all subsequent quench cycles a T_{max} temperature of 500 °C was implemented.

Given the postulated memory effect for hydrogen precipitation [32,69], the repeated cycling of dissolution and precipitation would likely impact upon the hydrogen solvi observed. It seems possible, however, that the presence of elevated temperature soaks would encourage the recovery of dislocations, thus reducing the propensity for heterogeneous nucleation at preferential sites, minimising the impact of repetitive cycles on solubility curves. The postulated damage recovery at temperatures present in this work is potentially supported by the reduction of irradiation induced dislocation loop density [70,71] and cold work dislocations [72] at similar temperatures.

The subsequent cycles, C2–C8, were based on raising the temperature above the TSSD of the sample and holding for 15 min to completely dissolve all hydrides. A quench was then performed using a sudden reduction in current to a level required to attain the isothermal dwell temperature present in each cycle. These actions were all performed automatically by the ETMT software using a pre-programmed operational plan. In practice, the loss of heat through radiation and conduction was not sufficient to instantaneously quench the sample, and the maximum rate of cooling was observed to be ≈ 30 °C s^{-1}. For the most significant quench, $\Delta T = 400$ °C, the time taken to reach the target temperature was ≈ 13.3 s. For this reason, all isothermal kinetics and strain observations were made starting from the initiation of the quench operation.

After a prolonged hold, the sample was cooled to T_{floor}, and hydrogen distribution checks were made along the axial length of the sample, between the grips. The hold temperatures implemented in the experimental design began at 100 °C and rose to 400 °C in increments of 50 °C. Given that the TSSP was found to be 361 °C, the final cycle, C8, demonstrated no detectable precipitation, and so it is excluded from any further analysis.

Cycle C7, the penultimate quench and hold operation, was modified to include a 1 °C s^{-1} ramp, intended to investigate the effect of multiple thermal cycles on dissolution solubility. Very little change in the TSSD curve was seen between the dissolution stages of cycles C1 and C7, well within the average experimental error of ± 15.5 $ppm_{wt.}$ seen in concentration throughout this programme. The average error in strain evolution was found to be $\pm 25.5 \times 10^{-6}$ determined from the prismatic lattice parameter and $\pm 173.9 \times 10^{-6}$ from the basal lattice parameter. The magnitude of these representative errors should be considered against the strains presented in all subsequent figures, so errors are given as absolute values rather than percentages. Note that the error in the basal lattice parameter derived strain is large compared to measured strains, and this introduces some uncertainty into the interpretation of the results for this plane. Fig. 2 contains a schematic diagram of all thermal operations that took place during this experiment.

The axial checks for hydrogen distribution, made at the T_{floor} temperature between each cycle, were performed owing to the fact that resistive heating leads to a thermal gradient across the sample between conductive contacts (in the RD), which is exacerbated by the loss of thermal energy into the water-cooled grips [73]. Additionally, the loss of heat from the sample surface into the chamber atmosphere could lead to the development of thermal gradients in the TD or ND, although these were considered second order to the axial gradient. Any thermal gradients have the potential to impact on the present experiment given the fact that hydrogen is known to have a strong propensity to diffuse to cooler regions, leading to depletion at the axial centre of the sample, where diffraction measurements are taken [5,74,75]. Checks indicated that while regions of enrichment and depletion did develop axially during the experiment, they were localised primarily to within 5 mm of the grips. The sample centre, where strain measurements were made, demonstrated only a small amount of depletion as a product of the

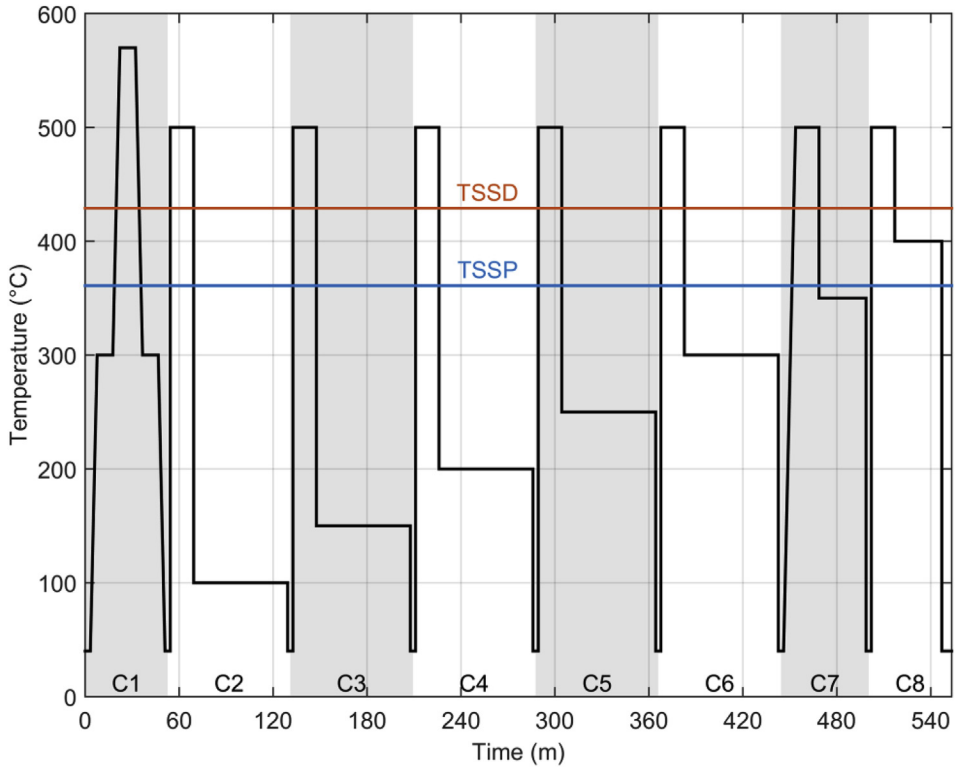

Fig. 2. Thermal Operations as a function of Time.

dwell cycles, by no more than ≈30 $ppm_{wt.}$, a value only marginally more than the average experimental error. Finally, at all times during the experiment a mass spectrometer was used to monitor the exhaust atmosphere of the ETMT chamber, with the intention of detecting any hydrogen desorption from the sample. This confirmed that no measurable quantity of hydrogen desorption was detected during the experiment.

2.4. Synchrotron data analysis

For measurements of diffracting volume of hydride, integration over the full azimuthal range of the Debye–Scherrer rings was performed, to ensure that diffraction from the maximum number of crystals of the precipitate was recorded. For strain analysis, however, partial integrations were used for the matrix and hydride in the four principle directions (considered 'compass points') of the Debye–Scherrer ring patterns. With the geometry of the sample–detector relationship, 0° and 180° represent the TD, while 90° and 270° represent the RD; these directions are illustrated in Fig. 1(b). The reason for using a narrow segment of the full pattern comes from the desire to give directionality to the recorded strain evolution. For the matrix, an integration with an azimuthal range of 15° ($\psi \pm 7.5$) was performed; however, the δ-hydride signal was low, so this sampling range was insufficient to resolve Bragg reflections. Instead, a partial integration with an azimuthal range of 45° ($\psi \pm 22.5$) was used for the hydride phase.

The diffractogram files produced by Fit2D were normalised as a function of beam intensity to remove the effect of synchrotron energy decay, after which they were simulated using TOPAS-Academic V5. Batch processing was handled using Matlab R2014b and a proprietary function. Instrumental broadening is accounted for by defining profile parameters from a Standard Reference Material and using these in the analysis of patterns recorded from the sample. Changes in profile shape can then be considered to arise predominantly from the sample, as instrument contributions are determined from the calibrant [76,77]. Consequently, any asymmetry or line broadening can be defined with parameters that consider the properties and structure of the sample.

A first attempt at batch diffraction pattern modelling utilised a Rietveld refined structural model [78,79] to give accurate weight percentage measurements. It was quickly observed that where hydride reflections were close to extinction, the software was not properly simulating these reflections. As an alternative method two boundary conditions were established, where complete signal extinction was taken to represent all hydrogen entering solution, while the intensity of the reflections at their maximum (and initial thermally un-cycled state) signified full precipitation. To support this, it can be seen from the work by McMinn that at the T_{floor} temperature the solubility of hydrogen is less than 1 $ppm_{wt.}$ [7], and so it is assumed throughout this work that all hydrogen has precipitated when close to room temperature. The combination of these two boundary conditions, along with an assumed linearity to the relationship linking integrated intensity of the hydride reflections and volume fraction, allows for the calculation of δ-hydride volume fraction from the recorded diffraction patterns.

In order to account for signal extinction, the Le Bail method [80] was employed to model both structures within TOPAS while batch processing. Unlike the Rietveld approach, reflection intensities are able to vary freely and independently of any texture parameters or one another [51]. Taking the values of cell mass from the Rietveld model and importing them into the Le Bail structure, TOPAS is then able to generate a nominal weight percentage for each phase. For reasons thought to be related to the free refinement of the scale parameter, allowed in order to grant the best possible fit for each modelled phase, these values were significantly different from the assumed boundary conditions. Using the boundary values, however, allows for the calibration of the weight percentage to represent the supposed true diffracting volume of hydride at any given point in the experiment. Additionally, the Le Bail model, like the Rietveld model, describes the spatial relationship between Bragg reflections as a function of crystal structure and lattice parameters. By refining the model to match the recorded pattern, sampling multiple reflections within the region of interest, it becomes possible to measure the lattice parameters of each phase present within imaged patterns. A representative example of the estimated standard deviation in a Le Bail refined lattice parameter for the hydride phase is 0.002 Å.

Fig. 3 demonstrates three patterns generated from a full (360°) azimuthal integration at key temperatures seen throughout the experimental programme; where the lattice spacing range represented on the x-axis is that which was modelled during data analysis. The hydride reflections shown were chosen due to their high multiplicities (24 for the $\{311\}_\delta$ and 12 for the $\{022\}_\delta$), along with being reasonably isolated from the tails of the dominant matrix reflections. The maximum intensities in these reflections, recorded in the material's initial state at 40 °C, are taken to represent 430 $ppm_{wt.}$ of hydrogen fully precipitated as hydride (or 100% precipitation). The high temperature data set shows no hydride reflections, and thus all hydrogen is treated as being in solution. The intermediate temperature plot, at 300 °C, shows partial precipitation, where the hydride intensity is half way between the high and low temperature boundary conditions.

Thermodynamic calculations to compute equilibrium solubilities were performed using JMatPro 7.0 in conjunction with the ZRDATA database. The MTEX 4.0 toolbox for Matlab was used for pole figure calculation and visualisation.

3. Results and discussion

3.1. Precipitation

A full investigation into the solubility and precipitation behaviour of hydrides during the isothermal holds is presented elsewhere [81]. The following, however, summarises the precipitation observations necessary to underpin the strain behaviour presented in this work. Fig. 4 illustrates the completion of the precipitation process as a function of time, during each of the dwells that took place during the experimental regime. Dashed vertical lines are included to show the time at which precipitation is considered to be complete for each series. From this figure, it is evident that for cycles C2 to C5 close to 98% of precipitation has occurred rapidly, within approximately the first 20–30 s, followed by a more gradual increase in completion. For the higher temperature cycles, C6 and C7, the driving force for precipitation is lower and so the process is slower, leading to increasing curvature in the data with elevating temperatures.

This additional time to completion is important, as dissolved deuterium occupying a tetrahedral site within the hexagonal close packed matrix unit cell leads to an ≈2.78 $Å^3$ volume expansion of the parent lattice [82]. A similar volume expansion can be expected for hydrogen, and thus when it leaves solution en-masse a net contraction (or negative lattice strain) will occur in the α zirconium phase, which will be reflected in the strain traces presented herein [51].

Another aspect to consider is the amount of hydrogen that forms hydrides at the end of each cycle, collated in Table 1 along with a calculated value for hydride volume percentage associated with each concentration. While these values are only a few percent, it is notable that the hydride volume of the alloy is more than 1.5% even at the highest dwell that showed precipitation (C7). This is

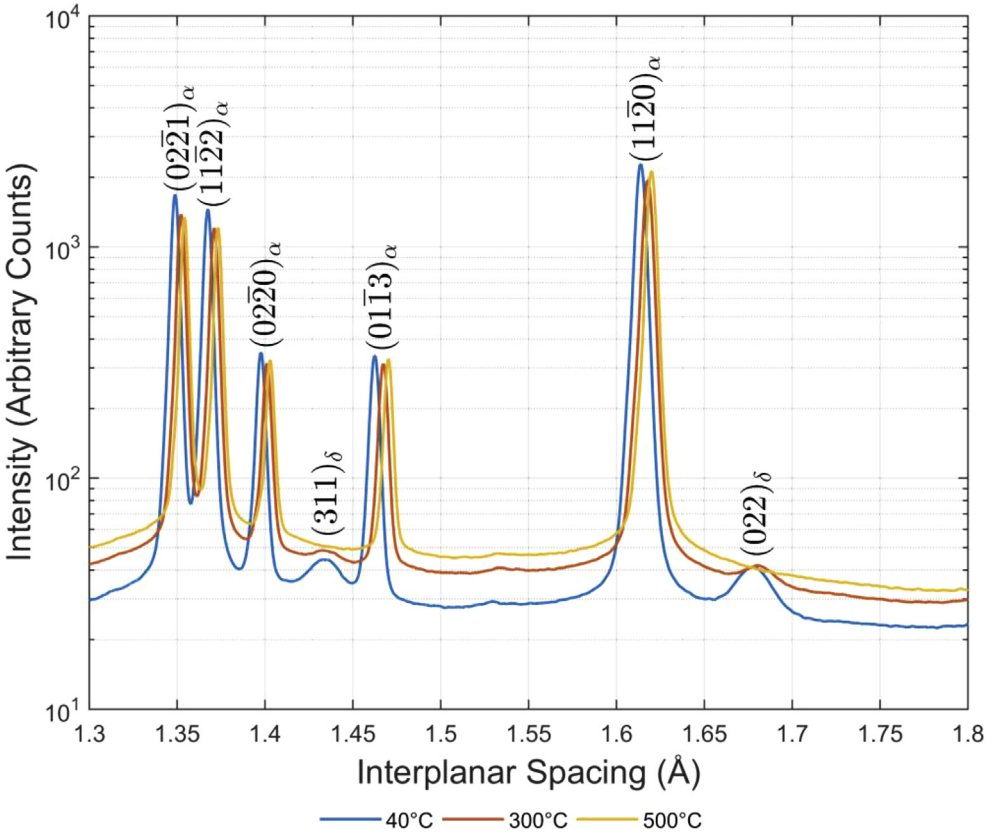

Fig. 3. Representative diffractograms from 40 °C, 300 °C and 500 °C acquisitions for the considered range of lattice spacing.

indicative of a steep increase in solubility between 350 °C and 400 °C (400 °C showing no precipitation), and highlights the non-negligible volume fraction of hydrides in each of the isothermal dwells. The importance of these observations will become evident later.

Lastly, the penultimate cycle (C7) was shorter than all others,

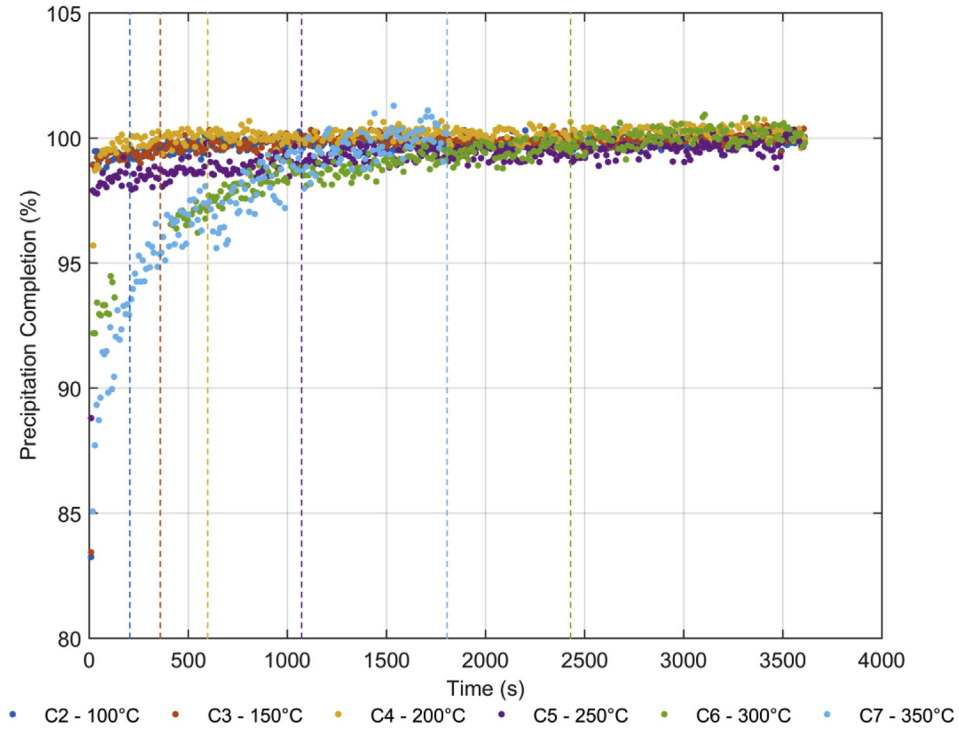

Fig. 4. Precipitation process completion as a function of time.

Table 1
Approximate precipitated hydride volume fractions at experimental dwell temperatures.

Temperature (°C)	Precipitated hydrogen concentration ($ppm_{wt.}$)	Approximate equivalent hydride volume fraction (%)
40	430	2.9
100	426	2.8
150	403	2.6
200	398	2.6
250	362	2.3
300	333	2.1
350	267	1.7
400	0	0

but the curvature of the precipitation trace is still significant up until the end of recording. Given the long time for the previous cycle (C6) to precipitate, it would appear likely that C7 was still some time away from completion, and was cut short by the experimental programme.

3.2. Texture

Before an investigation into the experimentally observed strains is performed, it is important to qualify the influence texture might have on these results. Given the recorded texture in Fig. 1(a), mechanical loading along RD would allow for easy activation of prismatic $\langle a \rangle$ slip, the slip mode with the lowest Critical Resolved Shear Stress (CRSS) [83]. Mechanical loading along the TD would promote a dominance of basal $\langle a \rangle$, and to a certain degree prismatic $\langle a \rangle$, slip. Finally, loading along ND requires activation of pyramidal $\langle c+a \rangle$ slip, which has a significantly higher CRSS [83]. These observations are reflected in the macroscopic stress–strain curves presented in Ref. [84], where yield stresses are lowest when deformed in the RD; although the effect appears more significant in compression than in tension in that work. This assessment is echoed by models in Ref. [83], where yield is lowest in the RD, followed by the TD and ND in sequence, owing to the texture of zirconium. Lastly, given that $\langle 0002 \rangle_{\alpha}$ is elastically stiffer than $< 11\bar{2}0 >_{\alpha}$ ($C_{11=22}^{11\bar{2}0_{\alpha}} = 142.63\ GPa$ and $C_{33}^{0002_{\alpha}} = 164.3\ GPa$ from the stiffness tensor in Ref. [85]), it may be possible that the greater degree of basal pole orientation in the TD could also mean that this direction might be marginally more elastically stiff, when compared with the RD.

3.3. Zirconium lattice strains

Matrix lattice strain evolution derivations are performed using relative changes in the prismatic and basal lattice parameters, which are calculated from the Le Bail model for the matrix and hydride phases. This approach allows for accurate calculations of unit cell parameter from sampling all reflections within the considered inter-planar spacing range of the diffraction pattern, Fig. 3, rather than using a single reflection analysis. It does, however, sample across the entirety of material of a phase within the gauge volume, so those reported matrix strains average across material close to hydrides (more misfit induced strain) and that further away (less strain). All strains presented in this work are relative, due to the formation of inter-granular stresses in α-zirconium, resulting from the significant anisotropy in the thermal expansion coefficients of the matrix, which prevents the accurate measurement of a_0 and c_0 values [51,86].

Fig. 5 contains separate subplots for the prismatic and basal lattice parameters, showing the strain evolution calculated for the end of each isothermal dwell in the rolling and transverse directions. Also included is the lattice dilatation resulting from thermal expansion in each lattice parameter calculated from a similar, but hydrogen-free, sample to illustrate the effect of hydrogenation on the zirconium lattice. Below each of the line plots is a series of bars that visualise the difference between the base thermal expansion and that recorded from a hydride sample. The evolution of matrix strain during a continuous heating ramp (C1 and C7) will be discussed in Section 3.4, when it will compared with strain in the hydride during the same thermal operation.

With the exception of 100 °C in the basal plot, the three lower temperatures in each subplot show close agreement with the expected thermally induced strain in each direction of the hexagonal close-packed unit cell. Of the basal parameter 100 °C points, it seems probable that because the material is both polycrystalline and possesses a strongly anisotropic unit cell, the inter-granular stresses that develop on cooling (from <a> and <c> thermal expansion mismatch) could constrain the basal inter-planar spacing, producing the lower than expected strain evolution that is observed. Above 200 °C, the recorded strain in both directions of the material departs from that predicted by thermal expansion alone, to an ever increasing degree. This deviation is the product of the increase in hydrogen solubility when moving towards higher temperatures, where the rise in dissolved hydrogen interstitially occupying the α-zirconium lattice leads to an expansion of the matrix unit cell [82].

A second feature of note within these subplots is that the TD consistently shows a higher degree of lattice dilatation than the RD. This might be the result of the texture, where a greater degree of basal poles oriented in the TD, as opposed to the RD (although the majority are actually in the ND), may cause a greater thermal strain in that direction for both the 'a' and 'c' parameters, from the interaction of neighbouring grains. Given this assessment, it might also be expected that the coefficients of thermal expansion should be different between the RD and TD, which is not apparent from Fig. 5, and so a clear cause for this systematic bias remains unclear.

In the following figures, plotted temporally, the initial data point at t = 0 s is taken as the final acquisition before the onset of the quench, and so a large initial thermally induced strain (up to $\approx 2000 \times 10^{-6}$) is recorded. Thermal contraction ceases to be a cause of strain evolution once the temperature, and thus lattice parameters, stabilise at the onset of the dwell. As the present evaluation is not concerned with thermally induced strains, and given the inability to calculate absolute matrix strains, all following strain traces are zeroed to the final value in each hold so that an assessment of strain evolution over the course of the isothermal dwell can be made, relative to their post-quench equilibrium state.

Figs. 6 and 7 show the recorded strain in the prismatic and basal lattice parameters for both the rolling and transverse directions of the α-zirconium lattice. The isothermal holds are divided into two groups, where Fig. 6 contains the three lower temperature cycles (C2–C4) and Fig. 7 contains the remaining upper temperature cycles (C5–C7). This is done for ease of interpretation, as it separates cycles into those that show rapid precipitation (under 750 s for those including and below 200 °C) and those showing slower precipitation (over 1000 s for 250 °C and higher).

Firstly, considering the low temperature cycles in Fig. 6, C2–C4, two distinct trends are apparent: the RD shows more elastic

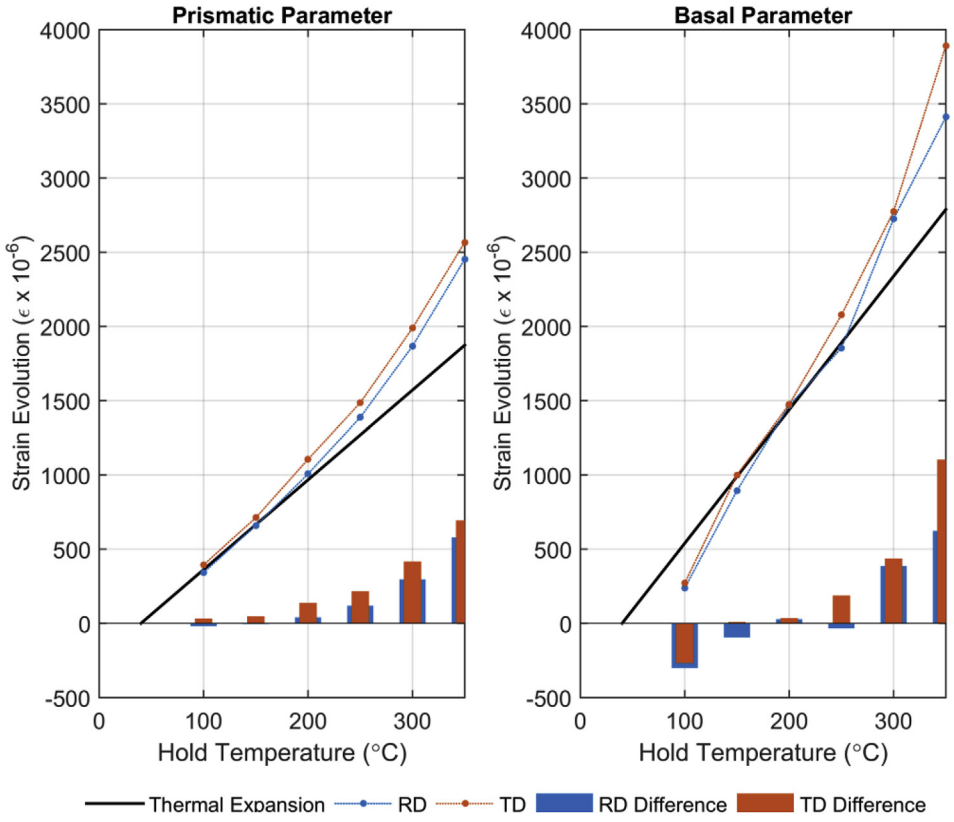

Fig. 5. Additional strain evolution present in the prismatic and basal lattice parameters of the zirconium matrix at the end of each isothermal hold, compared to base thermal expansion.

contraction than the TD, and the basal lattice parameter demonstrates more elastic strain evolution than the prismatic lattice parameter. In the following description, subplots are addressed in the order of least strain evolution to most.

Looking specifically at the prismatic TD subplot, the 150 °C and 200 °C traces (orange and yellow) indicate a very slight positive gradient, deviating from the trends observable in all other traces within this figure. The magnitude of this gradient is small, however, when compared to the measurement error, and so drawing conclusions from these two series should be done with caution. That being said, the formation of hydrides is thought to induce large compressive stresses within the precipitate, owing to the large misfit, so an equal balancing in the matrix with tensile stresses is also necessary. As such, a positive or dilative change in the lattice parameter may be indicative of stress balancing in these series, but is more plausibly attributed to experimental error. This is owed to the divergence of these series from the trends exhibited in other in this figure and also the low magnitude of the strains in question.

In the basal TD subplot, a modest amount of negative elastic strain evolution occurs during hydride formation, but appears to cease once the process of precipitation is considered complete (marked by vertical dashed lines for each series). From this point onwards, only noise fluctuations appears to occur up until the end of each cycle. For the prismatic RD data, continuous negative strain evolution is featured in all three series, and the cessation of precipitation appears to have little impact on the rate of strain evolution. Finally, the basal RD subplot shows a considerable amount of negative elastic strain evolution in all three cycles, occurring both during and after the period in which hydrides are known to form. In the 200 °C series, a potential change in gradient may be apparent close to the point of completion. Overall, increasing the precipitation temperature appears generally to decrease the amount of elastic strain evolution recorded during the dwell in all directions and both matrix parameters.

Fig. 7 shows a similar set of plots arranged in the same way as Fig. 6, but for the three higher temperature hold cycles. A gap exists in C6 where a storage ring top-up event occurred, which significantly destabilised recorded trends, and so a small portion of the data is excluded for clarity. Unlike the previous figure, precipitation continues well into each of these cycles, and so a like-for-like comparison with the previous set of three temperatures is difficult. Considering only the points after precipitation is completed (and discounting C7 entirely owing to its artificial shortening), very little strain evolution is observed for either of the lattice parameters and in any direction.

Given that a number of complex mechanisms are likely inducing strain in the matrix, it would not be prudent to analyse the recorded elastic strain evolution any further without attempting a deconvolution of the contributing components. For this reason, the equation describing lattice distortion resulting from solute hydrogen (from Zanellato et al. [51]), Equation (1), is used in conjunction with the tracked precipitation of hydrides to calculate the chemically induced lattice dilatation. Here, n_{Zr} is the number of zirconium atoms per unit cell, C_H^{at} is the dissolved molar hydrogen concentration, K is the coefficient of anisotropy, $\bar{v}_0$ is the initial cell volume, and Δv is the cell volume increase from interstitial deuterium (substituted in place of hydrogen). The resulting lattice contraction from interstitial hydrogen leaving solution to precipitate into hydrides is represented in Fig. 8.

$$\bar{\varepsilon}_a^d = \frac{n_{Zr} C_H^{at}}{\left(1 - C_H^{at}\right)(2+K)\bar{v}_0} \Delta v \tag{1}$$

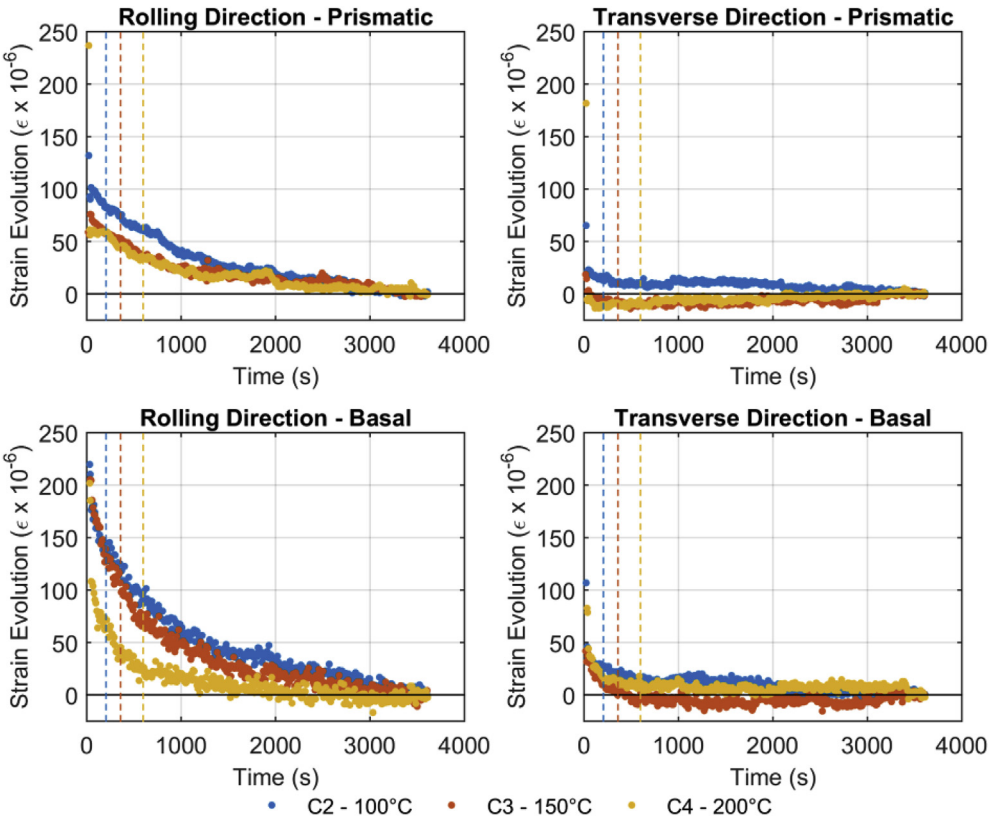

Fig. 6. Recorded relative strain evolution in the lattice parameters of the α-zirconium matrix during cycles C2–C4, where dashed vertical lines indicate the completion of precipitation at each temperature.

From the calculated chemical strains, it is evident that for the three lower temperature cycles, the effect of dissolved hydrogen on strain evolution is limited to the first 200–500 s. Past this time, both the prismatic and basal lattice parameters stabilise and only a degree of scatter appears within each trace. For the upper three cycles, where the kinetics of precipitation are rate limited by the chemical driving force for precipitation, the chemically induced negative strain evolution extends well into each dwell, as the result of the additional time it takes to complete the process of precipitation. The lowest temperature of these, C5, shows only a small magnitude of strain in the order of $\approx 30 \times 10^{-6}$, whereas the uppermost two cycles demonstrate as much as $\approx 150 \times 10^{-6}$ strain, owing to the significant change in the quantity of dissolved hydrogen. It should be noted, however, that these relative strains are normalised to zero at the end of each cycle, and so Fig. 8 only shows the change in chemically induced strain evolution that results from the precipitation occurring during each dwell period. The absolute value of the chemical dilatation at the end of each of these holds without this normalisation will be a positive value, because some amount of hydrogen will still remain in solution, dilating the α-lattice. Fig. 5 gives an indication of the magnitude of this effect, where the increase in strain above baseline thermal expansion is indicative of the strain induced by solute hydrogen.

Using the interstitial hydrogen induced negative lattice strain evolution, it becomes possible to remove the chemical contribution to strain from the data present in Figs. 6 and 7. Given that the temperature is stabilised by the third pattern acquisition (≈ 30 s) at the latest, any remaining elastic strain evolution past this point will likely be the sole product of mechanical phenomena within the sample induced by the misfit between hydride and the matrix. With this being said, Figs. 9 and 10 contain the derived mechanically induced elastic strain evolution during each dwell, separated as in previous figures. Unfortunately, this process effectively combines the noise present in the original recorded strain traces with that produced by the calculation for chemical dilatation, and so the magnitude of scatter present in these is larger than in previous figures. Nonetheless, the amounts of strain recorded, and the scatter in these values, remain very small. It should be noted that for simplicity it has been assumed that no change in stoichiometry of the hydride occurs, which would likely lead to another source of apparent strain [87]. Similarly, where a transformation from delta to gamma or vice versa would occur, a change in the misfit of each precipitate would then follow, which would impact upon the mechanical interaction, and may influence the resulting strains [34,41].

Considering first the three lower temperature cycles, Fig. 9, it is evident that there is still some degree of measurable strain evolution in the matrix for each of these temperatures, albeit predominantly in the RD of the material. The data for the TD show very little change overall in both the prismatic and basal lattice parameters. In all four subplots, mechanically induced strain evolution (that occurring after the precipitation complete dashed lines) ranges from essentially zero (prismatic and basal parameters in the TD) up to $\approx 150 \times 10^{-6}$ of negative elastic strain (basal parameter in the RD).

As hydrides form, the misfit of the particles is compressive [41], which must produce balancing tensile stresses in the matrix. These would be expected to continue to build as the precipitates grow and coarsen. Eventually, these stresses will reach the local yield stress of the material, and plastic relaxation will take place through the creation of dislocation structures. Where elastic strain evolution is seen in the lower temperature dwells after precipitation is complete, the mechanically induced lattice parameter strain evolution

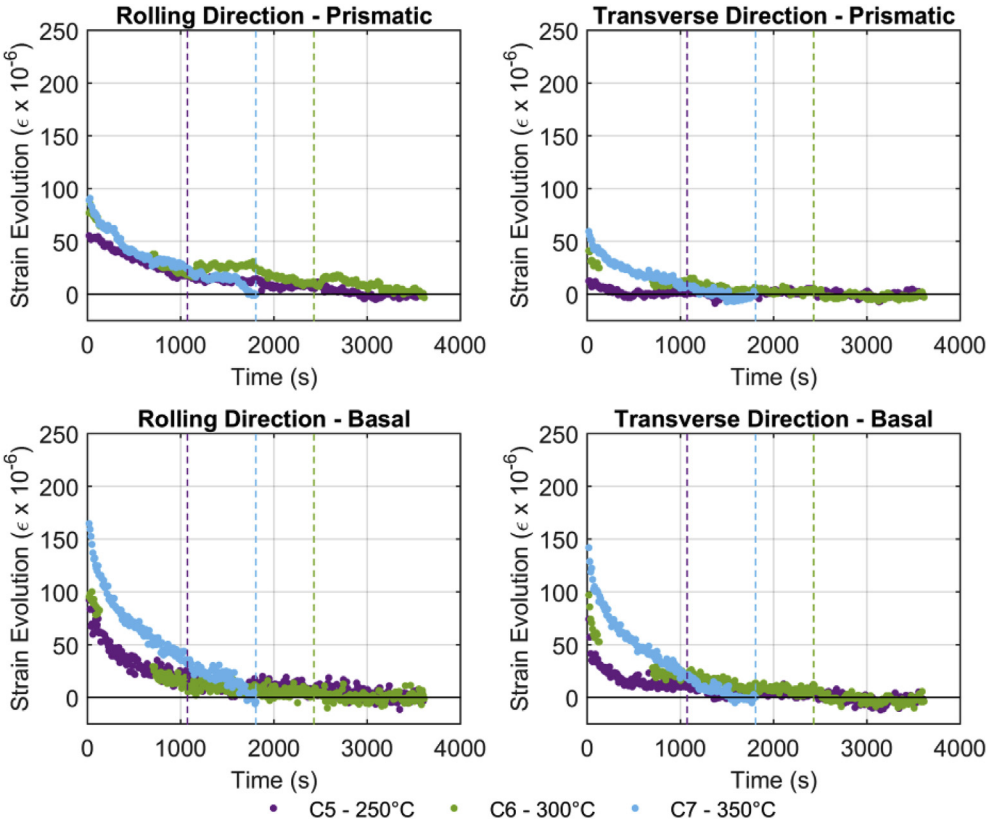

Fig. 7. Recorded relative strain evolution in the lattice parameters of the α-zirconium matrix during cycles C5–C7 where dashed vertical lines indicate the completion of precipitation at each temperature.

is negative with time during the dwell, before reaching equilibrium (taken as the 0 point in these plots). This indicates that a continuous, time dependent process seemingly takes place after precipitation, suggesting that slow strain rate plastic relaxation is in effect. The lack of observations in this work of dilative (tensile) strain evolution during precipitation is likely attributed to the rapid nature of precipitation, as in all series the vast majority (>85%) occurs within the first few (<3–4) data points, seen in Fig. 4. As such, the majority of misfit-related tensile strain evolution in the matrix would occur during the same period that the significantly more dominant thermal expansion strains would be causing the metallic lattice to contract, thus potentially masking them.

As $\langle 0002 \rangle_\alpha$ is stiffer than $<11\bar{2}0>_\alpha$, a recorded quantity of strain evolution in the basal inter-planar spacing will correspond to a larger stress relaxation than for the same strain recorded in $<11\bar{2}0>_\alpha$. Of the two lattice parameters, a greater degree of elastic strain relaxation is seen in $\langle 0002 \rangle_\alpha$, and so this corresponds to a significantly larger stress relaxation in this direction. The difference between $<11\bar{2}0>_\alpha$ and $\langle 0002 \rangle_\alpha$ strain magnitudes can be explained using the stress free transformation strains derived by Carpenter [41], or the interfacial strains measured by Barrow et al. [34].

In the case of Carpenter, the δ-hydride transformation strain is thought to be isotropic in $<11\bar{2}0>_\alpha$ and $<1\bar{1}00>_\alpha$ (4.58%), while the expansion in $\langle 0002 \rangle_\alpha$ is higher, at 7.2%, with a coefficient of anisotropy between the former pair and latter direction of 1.57 [41]. From Barrow, the interfacial strains in $<11\bar{2}0>_\alpha$ and $<1\bar{1}00>_\alpha$ measured from a formed precipitate (thus being the residual misfit strains after plastic relaxation has likely occurred) are anisotropic. The values reported by both authors are listed in Table 2.

From Barrow et al., the residual interfacial strain in $<1\bar{1}00>_\alpha$ is minimal, whereas those in the other two directions are substantially more, and the coefficient of transformation strain anisotropy between $<11\bar{2}0>_\alpha$ and $\langle 0002 \rangle_\alpha$ is 1.77. Given the high anisotropy between $\langle 0002 \rangle_\alpha$ and $<11\bar{2}0>_\alpha$ directions from both authors, the misfit between precipitate and parent lattice would be far greater in $\langle 0002 \rangle_\alpha$, thus generating larger stresses in this direction. Comparing the values from these two authors for the $\langle 0002 \rangle_\alpha$ direction suggests that the reduced misfit measured by Barrow et al. may be indicative of the degree of plastic relaxation that has taken place in this direction. This may then support the observation of notable elastic strain relaxation seen in the RD basal subplot.

Interestingly, the strong anisotropy between the residual misfit strains in $<11\bar{2}0>_\alpha$ and $<1\bar{1}00>_\alpha$ from Barrow et al. may go some way towards explaining why so little elastic strain evolution is seen in the TD of the material, when compared with the RD. From the measured specimen texture, Fig. 1(a), it can be seen that the $\{1\bar{1}00\}_\alpha$ poles are oriented predominantly in the RD direction, while the $\{11\bar{2}0\}_\alpha$ poles are oriented in the TD. The relatively low residual misfit reported in $<1\bar{1}00>_\alpha$ is thought to be the result of the incoherent nature of the interface in those directions [34], which likely acts as a source for dislocations that are needed to plastically relax the misfit strains in $<1\bar{1}00>_\alpha$. For the semi-coherent $<11\bar{2}0>_\alpha$ (the growth direction of needles), the tight radius of the tip aids in the accommodation of the misfit strain [34], and so less plastic relaxation would likely occur in those directions. This is manifest in a comparison of the predicted and observed strains reported in Table 1, where the difference between Barrow et al. and Carpenter is greater in the incoherent $<1\bar{1}00>_\alpha$ direction, than the coherent $<11\bar{2}0>_\alpha$ [34,41]. This direction, being that with greatest plastic relaxation of the misfit, being oriented predominantly in the RD (as a function of the texture) is then likely

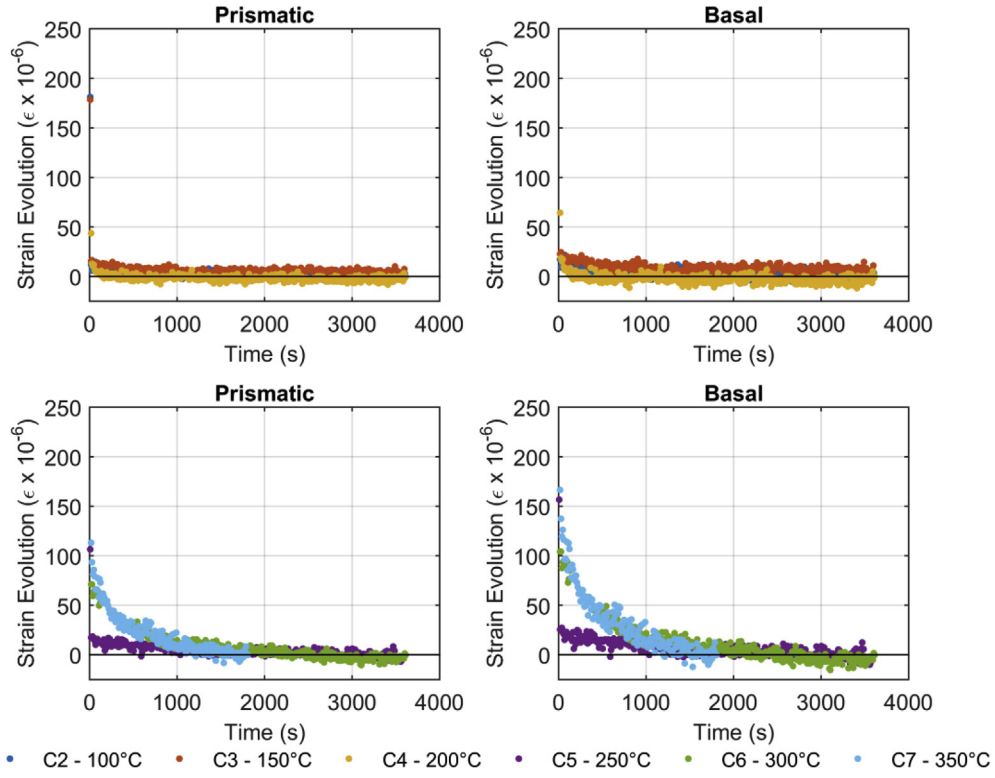

Fig. 8. Lattice contraction induced in α-zirconium from hydrogen leaving Solution.

why significant negative strains (thought to be indicative of relaxation) are also recorded in that direction in the present study.

From the data in Table 2, it is also evident that some relaxation of the misfit may also take place in $<11\bar{2}0>_{\alpha}$ (oriented in the TD), but no notable evidence of any time dependent relaxation is seen in Fig. 9 for the TD. It is thus suggested that any relaxation that does occur in $<11\bar{2}0>_{\alpha}$ does so while the process of precipitation is ongoing, rather than after it is complete. It should be noted that if this is the case, some fraction of the $<1\bar{1}00>_{\alpha}$ misfit likely also relaxes during precipitation, and so it is suggested that the post-precipitation relaxation encourages further relaxation of the misfit in $<1\bar{1}00>_{\alpha}$.

In other published work [51], the mechanical interaction between hydride and matrix has been considered second order owing to the low hydride volume fraction. This may be a fair assessment when the greatest magnitude seen is no more than $\approx 150 \times 10^{-6}$ strain, although it cannot be considered as entirely negligible during, or shortly after, the process of precipitation. Even though a maximum of only ≈2% of the diffracting volume of material is composed of precipitate, a clear mechanical interaction is seen on average in the metal matrix during the three lower temperature experimental dwells.

Of the higher temperature cycles, Fig. 10, the vast majority of experimentally recorded strain evolution is accounted for by hydrogen leaving solution, and so the matrix lattice strains presented show minimal change. The lowest temperature of these, the 250 °C dwell (purple), does show evidence of the same trends observed in the lower temperature cycles (Fig. 9), particularly in the RD. The 300 °C and 350 °C cycles, however, show essentially no mechanically induced strain evolution, and any deviations (such as that in series C7 within the basal RD subplot) are likely a mismatch between the modelled and recorded chemically induced strain. This seems unusual, considering that the misfit predicted by Singh et al. [87] becomes larger with increasing temperature, so it would be expected that this would produce larger stresses, and thus greater strain relaxation within the parent lattice at these temperatures.

This extra relaxation, however, is not seen in the present work, as hydrides take longer to form with raised temperature [81], so the excess stresses produced by the increased misfit may be relieved as quickly as they are produced while precipitation progresses. This is potentially exacerbated by the yield strength of the matrix being lower during these upper cycles, meaning that less stress is needed for plastic relaxation to ensue, and so it may begin much earlier in the precipitation process.

There are two final considerations to be made as to the validity of this assessment of matrix strain evolution, pertaining to the averaging of strains in the matrix and the source of strain. The presented strain evolution traces are based on the lattice parameters calculated from a Le Bail model of the α phase. These are, in turn, calculated from the centroid positions of the matrix reflections being sampled in the diffraction pattern, which are indicative of the average strain in the phase. Given that matrix strain arising from the misfit is non-uniform (in that it tails off rapidly with increasing distance from the precipitate), the Bragg reflections are essentially a composite of many smaller reflections, each representing a point on the strain gradient, the majority falling at the low strain end.

To cause a change in overall reflection centroids, the maximum magnitude of the misfit strain would need to be sufficiently large, such that it counteracts the far larger volume of material that experience minimal strain. To help mitigate this, increasing the quantity of local strain sources throughout the material could aid in maximising the volume of the matrix affected by it. This latter point may be helped by the thermal profile of the experiment, as it is known that rapid cooling to precipitate hydrides generally leads to a distribution of fine precipitates [88], which may help increase the volumetric coverage of the misfit strain fields. It should also be

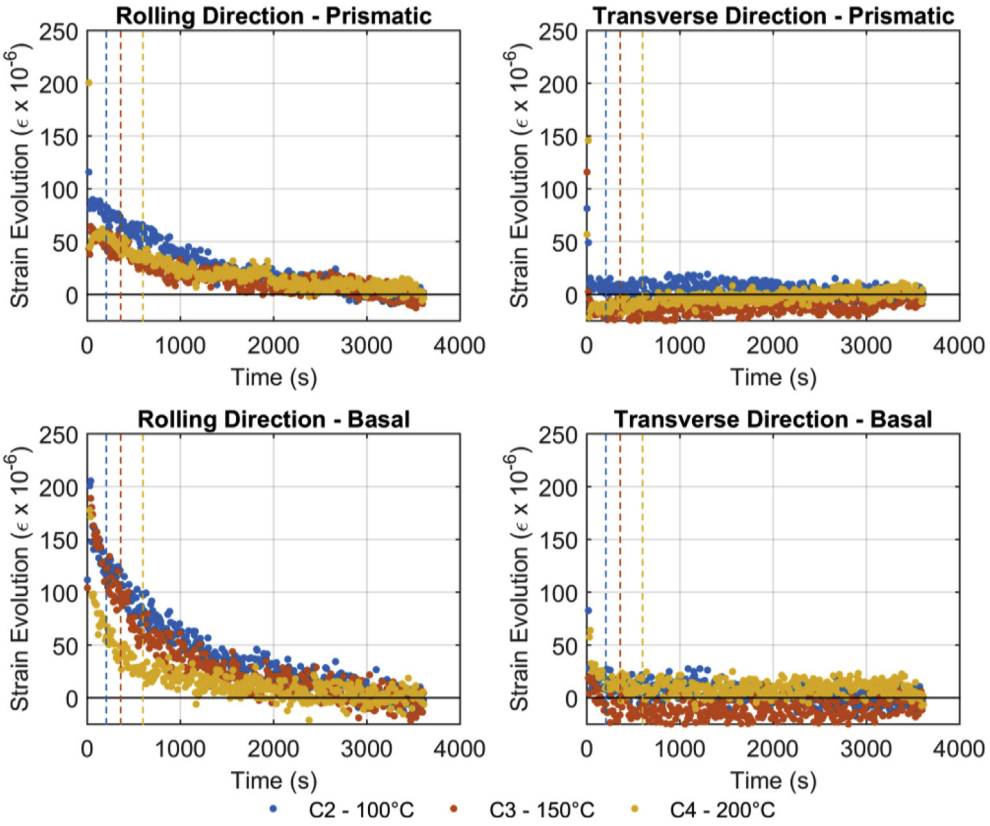

Fig. 9. Mechanically induced strain evolution in α-zirconium during lower temperature dwells, where dashed vertical lines indicate the completion of precipitation at each temperature.

remembered that the maximum mechanical strain relaxation being reported here is only $\approx 150 \times 10^{-6}$, or 0.015%, compared with the interfacial misfit strains given in Table 2 (up to 5.5% measured experimentally by Barrow et al. [34]), so it is not unrealistic that the relative strains reported in this work are in fact those averaged throughout the matrix.

With regard to the source of the observed strain evolution, it could be suggested that some mechanism related to the time-dependent release of hydrogen from trapping features may be responsible for the observed trends. Here, the dislocations, vacancies, or other features in the matrix that trap hydrogen can act to effectively increase the solubility of the material local to the traps, which, in turn, would increase the dilatation of the parent lattice in those regions. Were these traps to slowly release hydrogen, then the lattice would see negative strain resulting from hydrogen forming further hydrides, either within the traps themselves or from the excess solute hydrogen in the matrix, in order to maintain the equilibrium solubility.

There are two reasons that suggest that this alternate hypothesis may not be true, starting with the way in which precipitation might occur in the presence of hydrogen traps. It is known the dislocations left behind by dissolving hydrides act as traps for the hydrogen they release back into solution, and that on further precipitation the hydrogen saturated traps act to promote heterogeneous nucleation at these features, in a way known as the memory effect [69]. Given that the isothermal hold temperatures that see the most strain evolution in the present work are also those with the greatest driving force for precipitation, it seems likely that hydrogen in the traps would have formed hydrides rapidly after the quench, leaving few traps that might be able to release hydrogen. Were precipitation of trap released hydrogen to happen slowly over time, then the diffraction signal would show this through in increase in the intensity for the hydride phase, and as the present study reports strain evolution that occurs after the intensity has stabilised, it does not appear likely that further hydride is formed during the dwell. Additionally, the sensitivity for measuring precipitation completion is around 1% (5–6 $ppm_{wt.}$) when hydride reflections are developing, so the maximum strain evolution that could be unaccounted for due to noise in the intensity signal would be only $15–20 \times 10^{-6}$ and $22–28 \times 10^{-6}$ in the 'a' and 'c' parameters, respectively.

A second and more significant reason why the release of trapped hydrogen may not be the source of the recorded strain, however, is a feature of the four subplots in Fig. 9, namely the absence of any strain evolution in the TD. Were hydrogen to leave traps, the resulting lattice contraction would likely occur in both lattice parameters (to greater and lesser extents) and, significantly to this argument, in both processing directions, as there is a dilatational component in both $<11\bar{2}0>_\alpha$ and $<1\bar{1}00>_\alpha$. As there is none recorded in the TD, it is concluded that the presented matrix strain evolution is, indeed, likely a feature of the mechanical interaction between the misfitting precipitates and the parent lattice and not the slow release of trapped hydrogen.

3.4. Hydride lattice strain evolution

In a similar way as to follow the strain evolution in the matrix, it is also possible to track the hydride reflections within the interplanar spacing range of interest, Fig. 3, from which a lattice parameter for the phase can be calculated. This makes it possible to determine the strain evolution seen in the hydride. Before considering the isothermal dwell cycles, Fig. 11 displays the matrix

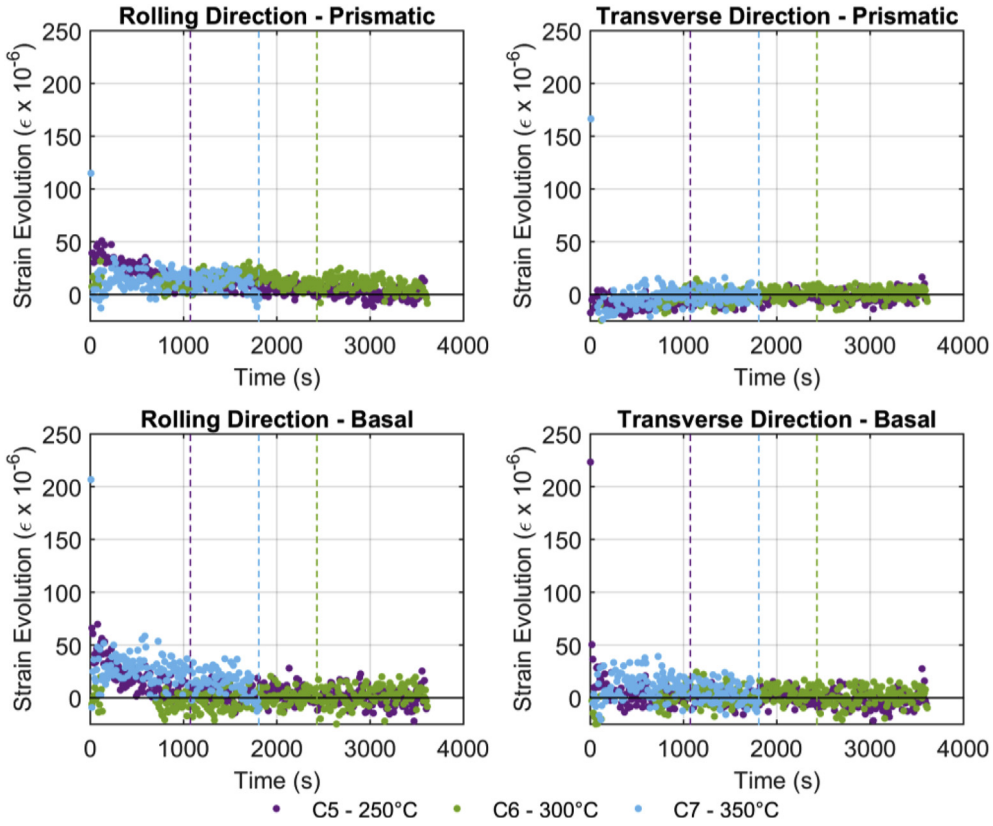

Fig. 10. Mechanically induced strain evolution in α-zirconium during higher temperature dwells, where dashed vertical lines indicate the completion of precipitation at each temperature.

Table 2
δ-Hydride stress fee transformation strains (carpenter)/interfacial strains (barrow) [34,41].

Direction	Carpenter	Barrow
$\langle 0002 \rangle_\alpha$	7.2%	5.5%
$< 11\bar{2}0 >_\alpha$	4.6%	3.1%
$< 1\bar{1}00 >_\alpha$	4.6%	0.5%

and hydride strain evolution measured along the RD and TD, as a function of temperature, during the initial (C1) and final (C7) 1 °C heating ramps. This allows for a deeper investigation into the interaction between matrix and hydride during continuous heating transients. For both phases and in both processing directions, the data can be separated into two distinct regions of lower and higher temperature separated at ≈280 °C, each with a different gradient. This kink is present in both the initial and final experimental cycles, and so it is believed to be inherent to the material, rather than introduced through experimental cycling (although a short thermal operation did occur pre-experiment). Additionally, the good degree of agreement between C1 (closed markers) and C7 (open markers) in all four subplots suggests a minimal impact of the aforementioned memory effect as the experiment progressed. This is likely attributed to the elevated temperature soaks allowing precipitation related matrix defects to recover somewhat, minimising the propensity for further heterogeneous nucleation at lattice defects produced by previously existing hydrides.

From the literature, the reported thermal expansion coefficient for bulk δ-hydride varies by a large margin, from author to author. For example, Yamanaka et al. report a range of 25 × 10^{-6} K^{-1} to 30 × 10^{-6} K^{-1} (based on stoichiometry) [89], while Kolas et al. report a lower value of 14.2 × 10^{-6} K^{-1} [40]. For comparison with the matrix, both of these sources present values that are significantly more than the values calculated for either of the matrix parameters from the current work. Here the prismatic and basal coefficients for the α phase are measured to be 6.04 × 10^{-6} K^{-1} and 8.97 × 10^{-1} K^{-1}, respectively, from a base metal sample containing no charged hydrogen and derived from a full 360° Debye–Scherrer ring integration. With these values in mind, the measured dilatation in the hydride phase in both upper subplots of Fig. 11, and over the entire thermal range, is significantly lower than would be expected from the literature sourced bulk hydride thermal expansion coefficients [40,89], which can be understood by considering that the hydrides are constrained by the metal matrix.

Below 280 °C the measured hydride expansion gradient in both processing directions is lower even than the smallest expansion coefficient of the matrix, however, the geometrical relationship between matrix and hydride unit cells must be considered before further assessment can be made. Given the known habit plane of $(0001)_\alpha \parallel (111)_\delta$ [90], the $\langle 100 \rangle_\delta$ family of directions, in which 'a' lattice parameter dilatation will occur, will not be aligned with the $< 11\bar{2}0 >_\alpha$ and $\langle 0002 \rangle_\alpha$ matrix directions, corresponding to the 'a' and 'c' lattice parameters, respectively. Instead, a comparison must be drawn between the $\langle 111 \rangle_\delta$ family of hydride directions and these two matrix directions, as seen in Fig. 12.

Taking the gradient of strain evolution for the hydride in the upper and lower temperature regions, it becomes possible to calculate the expansion in the $\langle 111 \rangle_\delta$ directions, presented in Table 3, where the linear regression to determine the gradient incorporates the uncertainties in lattice parameters calculated by TOPAS. From these values, the strain evolution in the $\langle 111 \rangle_\delta$ directions below 280 °C are similar to the matrix thermal expansion

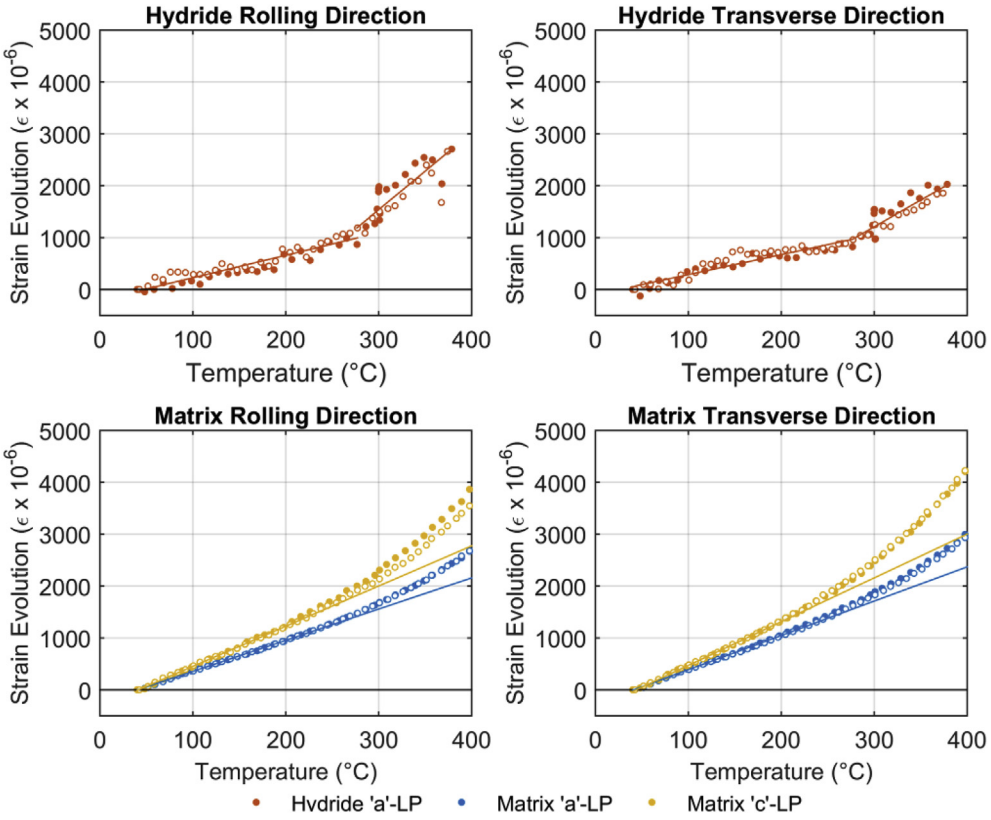

Fig. 11. Relative strain evolution recorded in the hydride (upper) and matrix (lower) lattice parameters, from the rolling and transverse directions of the sample during continuous 1 °C s^{-1} heating cycles (C1 – closed markers and C7 – open markers).

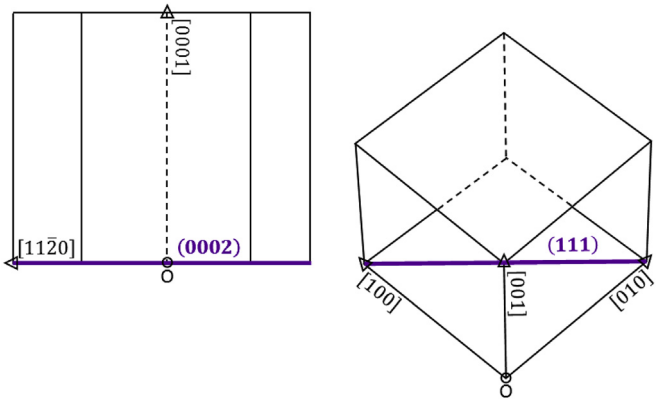

Fig. 12. Planar relationship between matrix (left) and hydride (right) unit cells.

coefficients (the $\langle 0002 \rangle_\alpha$ in the RD, and $<11\bar{2}0>_\alpha$ in the TD). The similarity between these parameters indicates that the matrix imposes significant constraint on the thermal expansion of the hydride in the lower thermal range. What is not clear, however, is why the $\langle 111 \rangle_\delta$ expansion shows close agreement with $\langle 0002 \rangle_\alpha$ in the RD, but the $<11\bar{2}0>_\alpha$ in the TD, although the margin of uncertainty for the $\langle 111 \rangle_\delta$ precludes a deeper assessment of whether this is true, or an artefact.

Above 280 °C the gradient of hydride expansion with temperature increases to a value that is larger than either of the thermal expansion coefficients for the matrix. In the TD, the value is still below the bulk hydride thermal expansion coefficient, suggesting that while the matrix is still constraining the precipitate, the effect is significantly lower in this thermal region. In the RD, however, the measured thermal strain coefficient shows good agreement with literature thermal expansion coefficients for the hydride phase from Yamanaka et al. [89], suggesting that minimal constraint is imposed by the matrix in this direction. This deviation between these two directions may be explained by the study of Barrow et al. [34], whereby the incoherent boundary (in the $<1\bar{1}00>_\alpha$ directions) oriented in the RD may encourage more plastic relaxation through slip in that direction, when compared with the TD, in which a semi-coherent boundary is oriented. This may then act to relax the matrix constraint on the hydride in the RD, while only partially relaxing it on the TD.

At elevated temperature, the observed reduction in the constraining effect of the matrix will also be partly the product of thermal softening, which will increase the ease of deformation system activation. From examining the strain in the matrix, however, it may seem possible that another mechanism might also be involved in reducing the constraint on the hydride. As the change in the gradient of evolved hydride strain coincides with the onset of significant chemically induced matrix lattice dilatation, it seems possible that the expansion of the parent lattice, caused by interstitial hydrogen, also allows an increase in hydride lattice expansion. Similarly, it is also conceivable that the progressive dissolution of hydrides with increasing temperature could also influence the constraint the phase experiences. It is suggested, however, that such an effect would follow the dissolution curve for hydrides, rather than manifesting as approximately linear regions separated by a kink, so this proposed source may be second order to the postulated chemical effect.

It should be noted, however, that this evaluation again assumes that no change in stoichiometry occurs in the hydride with

Table 3
Hydride $\langle 100 \rangle_\delta$ to $\langle 111 \rangle_\delta$ strain direction relationship, matrix $<11\bar{2}0>_\alpha$ and 0002_α directional thermal expansion, and associated uncertainties.

Material direction	Temperature region	Thermal strain ($\varepsilon \times 10^{-6}$)			
		$\langle 100 \rangle_\delta$	$\langle 111 \rangle_\delta$	$<11\bar{2}0>_\alpha$	$<0002>_\alpha$
RD	40–280 °C	4.32 ± 0.46	7.49 ± 0.80	6.00 ± 0.07	7.74 ± 0.12
RD	280 °C+	16.71 ± 2.87	28.93 ± 4.98	Non-Linear	
TD	40–280 °C	3.75 ± 0.40	6.49 ± 0.70	6.63 ± 0.11	8.44 ± 0.08
TD	280 °C+	10.20 ± 2.08	17.67 ± 3.59	Non-Linear	

increasing temperature, as does no change in phase stability. The importance of phase stability to the strain in the hydride is high, as the large difference between the misfit in the δ and γ phases would result in significantly different magnitudes of elastic and plastic deformation. Other authors [32,63,91,92] have reported a range of transformation temperatures for $\delta \rightleftharpoons \gamma$ interchange between 180 °C and 255 °C, the upper limit of which coincides well with the experimentally observed change in regime. It seems possible, then, that an alternate interpretation of this sharp step change may be a change from $\delta + \gamma$ below 260 °C to solely δ above it. The existence of a bimodal hydride phase distribution, where the misfit of γ needles is lower, might dilute the mechanical interaction with the parent matrix. This would lower the amount of plastic relaxation needed and increase the elastic constraining effect of the matrix.

Where only a single phase exists, the higher misfit of δ might increase plastic relaxation, thus reducing the constraining effect of the parent matrix and creating the increased gradient at higher temperatures. Barrow et al. [34] have reported evidence of composite precipitates that consist of needles with δ cores and γ tips, illustrating the potential complexity of the mechanisms driving this change [34]. During experimentation, however, no evidence of reflections belonging to another phase were observed within the recorded diffractograms. For this hypothesis to hold, the γ phase would have to exist in such low quantities as to not show any measurable diffraction signal, the gamma precipitates could be too fine to produce Bragg diffraction, or the γ phase could overlap heavily with the δ phase, thus making it impossible to deconvolute the two. It is highlighted that there would be γ reflections suitably isolated from those of δ, which would indicate the presence of this phase, but were not observed in the present study.

From the isothermal holds, Fig. 13 is produced, containing the evolution of the elastic strain for the hydride phase, separated into the two principle directions and the two temperature ranges being considered. In the lower temperature subplots, little elastic strain evolution is recorded, predominantly occurring before precipitation is complete. This would indicate that while the hydride lattice is able to dilate during the precipitation process, there is minimal elastic expansion after hydrides have fully formed. Of the higher temperature cycles, the hydride shows significant dilatation during the process of precipitation, possibly owing to the parent matrix being both elastically softer and yielding more easily, thus constraining the hydride to a lesser degree. It is possible that smaller precipitates forming at elevated temperatures could be less constrained by the matrix, but it is suggested that this would produce

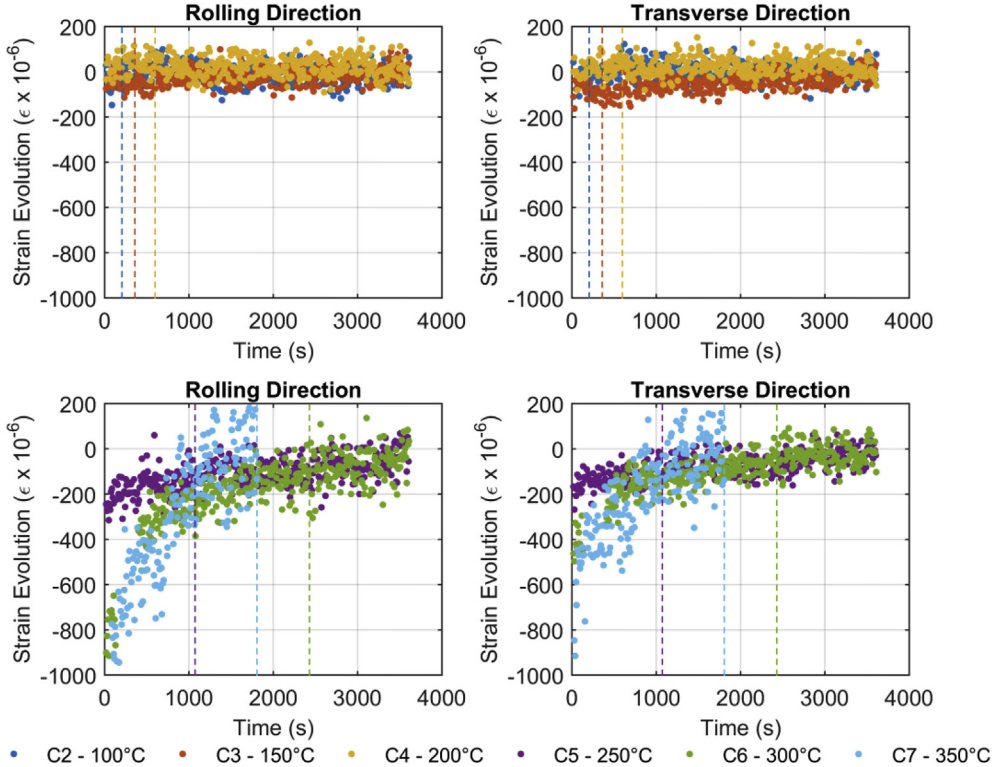

Fig. 13. Recorded relative strain evolution in the hydride lattice parameter during all isothermal holds (C2–C7), where dashed vertical lines indicate the completion of precipitation at each temperature.

lower initial stresses in the hydrides, rather than increasing the apparent dilative relaxation. Beyond the completion of precipitation, both C5 and C6 continue to show some small elastic expansion up to their final recorded/equilibrium state, suggesting a slow-strain rate relaxation effect could be taking place.

Elsewhere [40,58], it has been reported that hydrides are under some amount of compressive stress, which is likely true of newly formed precipitates or those that are continuing to grow. In those works, the temperature continues to decrease during measurements, leading to further precipitation of hydrides, introducing further stresses concurrent with thermally induced matrix hardening. Of hydrides formed isothermally under reactor operating conditions, however, it seems entirely possible that the softness of the matrix and slower rate of precipitation may allow the progressive relaxation of some portion of these stresses over an extended time period, through plastic deformation in the parent lattice. This could have ramifications for Delayed Hydride Cracking, where the failure of the hydride requires overcoming the 'shielding' compressive stress within the hydride, which result from the hydride misfit [93]. Should substantial stress relaxation take place in hydrides formed at under these conditions, it seems likely that the stress intensity required to cause hydride failure would also be reduced. As the strains recorded within the experiment are all relative, however, no comment on the absolute magnitude of stresses exerted on the hydride can be made. Interestingly, if slow-strain rate relaxation of hydride misfit stresses can occur, it seems plausible that high tensile stresses arising from other sources could also be relieved progressively over time. Applying this hypothesis to an example pertinent to DHC might suggest that the stresses arising from a sharp crack tip could encourage a gradual blunting of said defect through gradual plastic deformation.

Another interesting feature to note from the high temperature subplots in Fig. 13, is that unlike the matrix, where almost all elastic strain is recorded in the RD with little at all in the TD, the hydride shows considerable elastic expansion in both directions. This may be an artefact of the expanded integration of the Debye Scherrer patterns used for the hydride, where increasing the azimuthal range of the integration from 15° ($\psi \pm 7.5°$) to 45° ($\psi \pm 22.5°$) would increase the dilution of the RD strain evolution with an amount of that recorded in the TD, and vice versa. If not an artefact, the presence of hydride strain where there is none recorded in the matrix might indicate a change of stoichiometry or that coarsening of the hydrides is taking place. Here, growing precipitates would generate further plastic deformation in the surrounding metal, but the diffracting volume of hydride may not change in any recordable way, owing to smaller hydrides dissolving to feed larger ones. At this time, however, it remains unclear what the precise cause of this behaviour is.

4. Conclusion

An in-situ experimental programme investigating the δ-hydride and α-matrix phases was successfully able to monitor and track the evolution of very small strains during a series of thermal operations. The impacts of precipitation, along with matrix texture and hydride/matrix mechanical interactions, were evaluated as mechanisms underpinning the observed trends.

The introduction of hydrogen to zirconium induces a large amount of additional strain evolution in the matrix, echoing the observation of other authors that interstitial hydrogen causes significant lattice dilatation. Deconvolution was performed to separate the mechanical contribution to strain evolution from thermal and chemical effects. Mechanical strain was seen to be non-negligible during holds at temperatures of 100 °C–250 °C, where negative relative strains were observed during and after precipitation. These strains were thought to indicate slow strain rate relaxation of the misfit stresses.

The most significant matrix relaxation was observed in the RD, thought to be indicative of the incoherent $<1\bar{1}00>_\alpha$ hydride-matrix boundary being oriented in the RD, allowing for easier generation of dislocations and activation of slip. In the unit cell, the majority of strain evolution was observed in the basal lattice parameter, owing to the greatest misfit being oriented in that direction, and thus the highest stresses.

Of the 300 °C and 350 °C dwells, little mechanical relaxation was recorded, despite an expected misfit increase with temperature. This was explained through thermal softening preventing the build-up of significant misfit stresses, in conjunction with the longer times for hydrides to precipitate from a reduced chemical driving force.

During continuous heating transients, two distinct gradients were observed in the strain within the hydride, separated at around 280 °C. Below this, the thermal strain in the $\langle 111 \rangle_\delta$ was similar to the matrix thermal expansion coefficients. This was indicative of the matrix constraining the hydride, although no judgement could be made as to which planes in the matrix acted as the primary control.

An increase in hydride thermal strain was observed above 280 °C, where a gradient larger than either of the thermal expansion coefficients of the matrix was recorded. That in the RD matched a literature coefficient for hydride thermal expansion, but that from the TD did not. This was suggested to be linked to the proposed anisotropy in misfit relaxation between the $<1\bar{1}00>_\alpha$ and $<11\bar{2}0>_\alpha$ directions, related to the coherency of the interfaces in these directions and their ease of activating plastic deformation. The reduction in constraint at elevated temperature was suggested as being due to a combination of thermal softening and matrix lattice dilatation caused by an increase in interstitial hydrogen, although the possible influence of dissolution was also considered.

During isothermal holds, little elastic strain evolution is observed in the hydride during the lower experimental temperatures, occurring mainly during precipitation. At higher temperatures, significant elastic dilatation is seen during precipitation, likely indicative of an elastically softer and weaker matrix constraining the hydride less. After precipitation is complete, a slow strain rate relaxation effect was seen, suggesting that at reactor operating conditions hydrides may be capable of relaxing some degree of internal compressive stresses over time.

Acknowledgements

The author would like to thank the Institut de Radioprotection et de Sûreté Nucléaire for funding the beam time and providing the samples utilised in this experiment as well as Rolls-Royce and the Engineering and Physical Sciences Research Council for providing sponsorship funding (EP/I003290/1, EP/I005420/1). Further acknowledgements should be given to the infrastructural support of the Materials Performance Centre at The University of Manchester, and the University as a whole. The author is also grateful to J. Blomqvist and T. Maimaitiyili of the University of Malmö for helpful two-way exchanges of technique and best practice for synchrotron analysis. Finally, thanks should be given to A.T.W. Barrow, of Rolls-Royce, S.C. Connolly, of Oxford University, and S.R. Ortner, of the National Nuclear Laboratory, for technical guidance and discussions assisting the preparation of this work for publication.

References

[1] D.O. Northwood, Mater. Des. 6 (1985) 58.
[2] M. Kerr, M.R. Daymond, R.A. Holt, J.D. Almer, J. Nucl. Mater. 380 (2008) 70.

[3] M. Yamamoto, S. Naito, M. Mabuchi, T. Hashino, J. Phys. Chem. 96 (1992) 3409.
[4] B. Cox, Mechanisms of Hydrogen Absorption by Zirconium Alloys, 1984.
[5] B. Cox, P. Rudling, IZNA-1 SPECIAL TOPICS REPORT: Hydriding Mechanisms and Impact on Fuel Performance, Surahammar, Sweden, 2004.
[6] A.V. Nero, Am. J. Phys. 48 (1980) 327.
[7] A. McMinn, E.C. Darby, J.S. Schofield, in: P. Sabol, G.D. Moan (Eds.), Zircon. Nucl. Ind. Twelfth Int. Symp., American Society for Testing and Materials, West Conshohocken, PA, 2000, pp. 173–195.
[8] H. Weidinger, in: 6. Int. Conf. WWER Fuel Performance, Model. Exp. Support, Albena, Bulgaria, 2006, p. 20.
[9] S.B. Wisner, R.B. Adamson, Nucl. Eng. Des. 185 (1998) 33.
[10] K.W. Lee, S.I. Hong, J. Alloys Compd. 346 (2002) 302.
[11] H.-H. Hsu, L.-W. Tsay, J. Nucl. Mater. 408 (2011) 67.
[12] W. Qin, J.A. Szpunar, N.A.P. Kiran Kumar, J. Kozinski, Acta Mater. 81 (2014) 219.
[13] W. Qin, J.A. Szpunar, J. Kozinski, Acta Mater. 60 (2012) 4845.
[14] S. Arsene, J.B. Bai, P. Bompard, Metall. Mater. Trans. A 34 (2003) 553.
[15] W. Yeniscavich, R.A.A. Wolfe, R.M.M. Lieberman, J. Nucl. Mater. 1 (1959) 271.
[16] S.C. Lin, M. Hamasaki, Y.D. Chuang, Y.M. Hamasaki, D. Chuang, Nucl. Sci. Eng. 71 (1979) 251.
[17] P. Adelfang, V. Inozemtsev, Delayed Hydride Cracking of Zirconium Alloy Fuel Cladding, 2010. Vienna, Austria.
[18] P. Efsing, K. Pettersson, in: Zircon. Nucl. Ind. Twelfth Int. Symp., American Society for Testing and Materials, West Conshohocken, PA, 2000.
[19] I.G. Ritchie, C.E. Coleman, M. Roth, V. Grigoriev, Delayed Hydride Cracking in Zirconium Alloys in Pressure Tube Nuclear Reactors, International Atomic Energy Agency, Vienna, Austria, 2004.
[20] Y. Kim, S. Kim, J. Nucl. Mater. 270 (1999) 147.
[21] V. Macdonald, D. Le Boulch, A.H. de Menibus, J. Besson, Q. Auzoux, J. Crépin, T. Le Jolu, Procedia Mater. Sci. 3 (2014) 233.
[22] A. Hellouin de Menibus, Q. Auzoux, O. Dieye, P. Berger, S. Bosonnet, E. Foy, V. Macdonald, J. Besson, J. Crépin, J. Nucl. Mater. 449 (2014) 132.
[23] G.A. McRae, C.E. Coleman, B.W. Leitch, J. Nucl. Mater. 396 (2010) 130.
[24] Y.S. Kim, J. Nucl. Mater. 399 (2010) 240.
[25] M.P. Puls, J. Nucl. Mater. 399 (2010) 248.
[26] Y.S. Kim, J. Nucl. Mater. 399 (2010) 259.
[27] A. Steuwer, J.R. Santisteban, M. Preuss, M.J. Peel, T. Buslaps, M. Harada, Acta Mater. 57 (2009) 145.
[28] H. Okamoto, J. Phase Equilib. Diffus. 27 (2006) 548.
[29] B. Nath, G.W. Lorimer, N. Ridley, J. Nucl. Mater. 58 (1975) 153.
[30] C.D. Cann, E.E. Sexton, Acta Metall. 28 (1980) 1215.
[31] C.D. Cann, M.P. Puls, E.E. Sexton, W.G. Hutchings, J. Nucl. Mater. 126 (1984) 197.
[32] J.H. Root, W.M. Small, D. Khatamian, O.T. Woo, Acta Mater. 51 (2003) 2041.
[33] L. Barrow, A.T.W. Barrow, J. Almer, M.R. Daymond, J. Nucl. Mater. 442 (2013) 292.
[34] A.T.W. Barrow, A. Korinek, M.R. Daymond, J. Nucl. Mater. 432 (2013) 366.
[35] R.S. Daum, Y.S. Chu, A.T. Motta, J. Nucl. Mater. 392 (2009) 453.
[36] Z. Zhao, J.P. Morniroli, A. Legris, A. Ambard, Y. Khin, L. Legras, M. Blat-Yrieix, J. Microsc. 232 (2008) 410.
[37] J. Xu, S.-Q. Shi, J. Nucl. Mater. 327 (2004) 165.
[38] Z. Zhao, M. Blat-Yrieix, J.-P. Morniroli, A. Legris, L. Thuinet, Y. Kihn, A. Ambard, L. Legras, M. Limback, B. Kammenzind, S.W. Dean, J. ASTM Int. 5 (2008) 101161.
[39] J. Blomqvist, J. Olofsson, A. Alvarez, C. Bjerken, in: 15th Int. Conf. Environ. Degrad. Mater. Nucl. Power Syst. React., John Wiley & Sons, Hoboken, New Jersey, Canada, 2012.
[40] K.B. Colas, A.T. Motta, M.R. Daymond, M. Kerr, J.D. Almer, P. Barberis, S.W. Dean, J. ASTM Int. 8 (2011) 103033.
[41] G.J.C. Carpenter, J. Nucl. Mater. 48 (1973) 264.
[42] B.F. Kammenzind, B.M. Berquist, R. Bajaj, P.H. Kreyns, D.G. Franklin, in: Zircon. Nucl. Ind. Twelfth Int. Symp., American Society for Testing and Materials, West Conshohocken, PA, 1998.
[43] V. Perovic, G.C. Weatherly, C.J. Simpson, Acta Metall. 31 (1983) 1381.
[44] B. Cox, J. Alloys Compd. 256 (1997) L4.
[45] G.B. Allen, M. Kerr, M.R. Daymond, J. Nucl. Mater. 430 (2012) 27.
[46] V. Perovic, G.R. Purdy, L.M. Brown, Acta Metall. 29 (1981) 889.
[47] D.G. Westlake, J. Nucl. Mater. 26 (1968) 208.
[48] N.A.P. Kiran Kumar, J.A. Szpunar, Mater. Sci. Eng. A 528 (2011) 6366.
[49] C.E. Ells, J. Nucl. Mater. 28 (1968) 129.
[50] J.S. Bradbrook, G.W. Lorimer, N. Ridley, J. Nucl. Mater. 42 (1972) 142.
[51] O. Zanellato, M. Preuss, J.-Y. Buffiere, F. Ribeiro, A. Steuwer, J. Desquines, J. Andrieux, B. Krebs, J. Nucl. Mater. 420 (2012) 537.
[52] N.A.P. Kiran Kumar, J.A. Szpunar, Z. He, J. Nucl. Mater. 403 (2010) 101.
[53] N.E. Paton, B.S. Hickman, D.H. Leslie, Metall. Trans. 2 (1971) 2791.
[54] M.P. Puls, Acta Metall. 29 (1981) 1961.
[55] P. Vizcaíno, J.R. Santisteban, M.A. Vicente Alvarez, A.D. Banchik, J. Almer, M.A.V. Alvarez, A.D. Banchik, J. Almer, J. Nucl. Mater. 447 (2014) 82.
[56] J.H. Root, R.W.L. Fong, J. Nucl. Mater. 232 (1996) 75.
[57] A.T.W. Barrow, C. Toffolon-Masclet, J. Almer, M.R. Daymond, J. Nucl. Mater. 441 (2013) 395.
[58] J.R. Santisteban, M.A. Vicente-Alvarez, P. Vizcaíno, A.D. Banchik, J.D. Almer, Acta Mater. 58 (2010) 6609.
[59] K.B. Colas, A.T. Motta, M.R. Daymond, J.D. Almer, J. Nucl. Mater. 440 (2013) 586.
[60] K.B. Colas, A.T. Motta, J.D. Almer, M.R. Daymond, M. Kerr, A.D. Banchik, P. Vizcaino, J.R. Santisteban, Acta Mater. 58 (2010) 6575.
[61] M. Kerr, M.R. Daymond, R. a. Holt, J.D. Almer, S. Stafford, K.B. Colas, Scr. Mater. 61 (2009) 939.
[62] M. Kerr, M.R. Daymond, R.A. Holt, J.D. Almer, S. Stafford, Scr. Mater. 62 (2010) 341.
[63] E. Tulk, M. Kerr, M.R. Daymond, J. Nucl. Mater. 425 (2012) 93.
[64] Y.N. Wang, J.C. Huang, Mater. Chem. Phys. 81 (2003) 11.
[65] J.A. Gruber, S.A. Brown, G.A. Lucadamo, J. Nucl. Mater. 408 (2011) 176.
[66] T. Tschentscher, P. Suortti, J. Synchrotron Radiat. 5 (1998) 286.
[67] P. Suortti, T. Buslaps, P. Fajardo, V. Honkimäki, M. Kretzschmer, U. Lienert, J.E. McCarthy, M. Renier, A. Shukla, T. Tschentscher, T. Meinander, J. Synchrotron Radiat. 6 (1999) 69.
[68] P. Vizcaíno, C.P. Fagundez, A.D. Banchik, Engineering 02 (2010) 573.
[69] D.J. Cameron, R.G. Duncan, J. Nucl. Mater. 68 (1977) 340.
[70] J. Ribis, F. Onimus, J.-L. Béchade, S. Doriot, A. Barbu, C. Cappelaere, C. Lemaignan, J. Nucl. Mater. 403 (2010) 135.
[71] R.B. Adamson, W.L. Bell, in: Proc. Int. Symp. Microstruct. Mech. Behav. Mater., Xi'an, People's Republic of China, 1985, p. 237.
[72] B.M. Pande, M.S. Anand, R.P. Agarwala, Phys. Status Solidi 10 (1972) K137.
[73] M. Andreas, Effect of Different Loading Conditions on the Accumulation of Residual Strain in a Creep Resistant 1% CrMoV Steel – a Neutron and X-ray Diffraction Study PAR, École Polytechnique Fédérale de Lausanne, 2013.
[74] H.S. Hong, S.J. Kim, K.S. Lee, J. Nucl. Mater. 257 (1998) 15.
[75] A. Sawatzky, J. Nucl. Mater. 2 (1960) 321.
[76] D. Balzar, N. Audebrand, M.R. Daymond, A. Fitch, A. Hewat, J.I. Langford, A. Le Bail, D. Louër, O. Masson, C.N. McCowan, N.C. Popa, P.W. Stephens, B.H. Toby, J. Appl. Crystallogr. 37 (2004) 911.
[77] R.W. Cheary, A.A. Coelho, J.P. Cline, J. Res. Inst. Stand. Technol. 109 (2004) 1.
[78] L.B. McCusker, R.B. Von Dreele, D.E. Cox, D. Louër, P. Scardi, J. Appl. Crystallogr. 32 (1999) 36.
[79] H.M. Rietveld, J. Appl. Crystallogr. 2 (1969) 65.
[80] A. Le Bail, Powder Diffr. 20 (2005) 316.
[81] M.S. Blackmur, J.D. Robson, M. Preuss, O. Zanellato, R.J. Cernik, S.-Q. Shi, F. Ribeiro, J. Andrieux, J. Nucl. Mater. 464 (2015) 160.
[82] S.R. MacEwen, C.E. Coleman, C.E. Ells, J. Faber Jr., Acta Metall. 33 (1985) 753.
[83] F. Xu, R.A. Holt, M.R. Daymond, Acta Mater. 56 (2008) 3672.
[84] S. Cai, M.R. Daymond, R.A. Holt, Acta Mater. 57 (2009) 407.
[85] H.S. Rosenbaum, J.E. Lewis, J. Nucl. Mater. 67 (1977) 273.
[86] S.R.R. MacEwen, C. Tome, J. Faber, Acta Metall. 37 (1989) 979.
[87] R.N. Singh, P. Ståhle, A.R. Massih, A.A. Shmakov, J. Alloys Compd. 436 (2007) 150.
[88] B.A. Cheadle, C.E. Coleman, M. Ipohorski, in: Zircon. Nucl. Ind. 6th Int. Symp., American Society for Testing and Materials, 1984, pp. 210–221.
[89] S. Yamanaka, K. Yoshioka, M. Uno, M. Katsura, H. Anada, T. Matsuda, S. Kobayashi, J. Alloys Compd. 293–295 (1999) 23.
[90] K. Une, K. Nogita, S. Ishimoto, K. Ogata, J. Nucl. Sci. Technol. 41 (2004) 731.
[91] S. Mishra, K.S. Sivaramakrihnan, M.K. Asundi, J. Nucl. Mater. 45 (1972) 235.
[92] W.M. Small, J.H. Root, D. Khatamian, J. Nucl. Mater. 256 (1998) 102.
[93] M.P. Puls, in: Eff. Hydrog. Hydrides Integr. Zircon. Alloy Components, Springer London, London, 2012.